THE SPECTRUM OF THE RECYCLED PSR J0437−4715 AND ITS WHITE DWARF COMPANION

Martin Durant[1], Oleg Kargaltsev[1], George G. Pavlov[2,3], Piotr M. Kowalski[4], Bettina Posselt[2],
Marten H. van Kerkwijk[5], and David L. Kaplan[6,7]

[1] Department of Astronomy, University of Florida, FL 32611-2055, USA; martin.durant@astro.ufl.edu
[2] Department of Astronomy and Astrophysics, Pennsylvania State University, PA 16802, USA
[3] St. Petersburg Polytechnical University, Polytechnicheskaya ul. 29, St. Petersburg 195257, Russia
[4] Helmholtz Centre Potsdam–GFZ German Research Centre for Geosciences, Telegrafenberg, 14473 Potsdam, Germany
[5] Department of Astronomy, University of Toronto, 50 St. George Street, Toronto, ON M5S 3H4, Canada
[6] Physics Department, University of Wisconsin–Milwaukee, Milwaukee, WI 53211, USA
[7] Kavli Institute for Astrophysics and Space Research and Department of Physics, Massachusetts Institute of Technology, Cambridge, MA 02139, USA

ABSTRACT

We present extensive spectral and photometric observations of the recycled pulsar/white dwarf binary containing PSR J0437−4715, which we analyzed together with archival X-ray and gamma-ray data, to obtain the complete mid-infrared to gamma-ray spectrum. We first fit each part of the spectrum separately, and then the whole multi-wavelength spectrum. We find that the optical–infrared part of the spectrum is well fit by a cool white dwarf atmosphere model with pure hydrogen composition. The model atmosphere ($T_{\rm eff} = 3950 \pm 150$ K, $\log g = 6.98 \pm 0.15$, $R_{\rm WD} = (1.9 \pm 0.2) \times 10^9$ cm) fits our spectral data remarkably well for the known mass and distance ($M = 0.25 \pm 0.02\ M_\odot$, $d = 156.3 \pm 1.3$ pc), yielding the white dwarf age ($\tau_{\rm WD} = 6.0 \pm 0.5$ Gyr). In the UV, we find a spectral shape consistent with thermal emission from the bulk of the neutron star surface, with surface temperature between 1.25×10^5 and 3.5×10^5 K. The temperature of the thermal spectrum suggests that some heating mechanism operates throughout the life of the neutron star. The temperature distribution on the neutron star surface is non-uniform. In the X-rays, we confirm the presence of a high-energy tail which is consistent with a continuation of the cutoff power-law component ($\Gamma = 1.56 \pm 0.01$, $E_{\rm cut} = 1.1 \pm 0.2$ GeV) that is seen in gamma rays and perhaps even extends to the near-UV.

Key words: binaries: general – pulsars: individual (PSR J0437−4715) – white dwarfs – X-rays: binaries

Online-only material: color figures

1. INTRODUCTION

Millisecond pulsars (MSPs) are neutron stars that have been spun up through the accretion of matter from the binary companion at some time in the past, as part of a binary system. This process, known as recycling, enables the pulsar to emit detectable emission long after it would have died as a classical pulsar.

MSPs have mainly been observed in the radio, where the emission is dominated by coherent processes, and in X-rays and γ-rays. The X-ray radiation is thought to comprise two components: non-thermal emission from the magnetosphere, which is characterized by hard spectra (photon index $\Gamma = 1$–2) and sharp pulsations with high pulsed fraction; and thermal, surface emission, which has softer spectra and smoother pulsations. The former mechanism dominates in MSPs with high spin-down luminosity[8] $\dot{E} > 10^{35}$ erg s^{-1} (e.g., PSR B1821−24 and B1937+21), whereas a second group of MSPs with $\dot{E} = 10^{33}$–10^{34} erg s^{-1} (e.g., PSR J0030+0451) show mainly thermal emission, with a possible power-law (PL) high-energy component. For thermal spectra, X-ray observations are most sensitive to temperatures $T \sim$ few$\times 10^6$ K, which are considered to be typical temperatures for MSP polar caps, heated by relativistic particles.

PSR J0437−4715 is an MSP ($P = 5.8$ ms) in a binary system with a white dwarf (WD), with orbital period 5.5 days. Bell et al. (1995) measured the proper motion of PSR J0437−4715, 135 ± 4 mas yr^{-1} and detected an H$_\alpha$

bow-shock nebula in the approximate direction of motion; later Deller et al. (2008) greatly improved the accuracy of the proper motion measurements using very long baseline interferometry (VLBI; $\mu_\alpha = 121.679 \pm 0.052$ mas yr^{-1}, $\mu_\delta = -71.820 \pm 0.086$ mas yr^{-1}), and provided the most accurate distance to PSR J0437−4715, $d = 156.3 \pm 1.3$ pc (making it one of the closest pulsars known). The masses of the two binary components are $M_{\rm PSR} = 1.76 \pm 0.20\ M_\odot$; $M_{\rm WD} = 0.254 \pm 0.018\ M_\odot$ (Verbiest et al. 2008), and the orbital inclination $i = 137\overset{\circ}{.}6 \pm 0\overset{\circ}{.}2$. PSR J0437−4715 is the brightest of the MSPs in the UV and X-rays. Detailed spectral studies have suggested that the bulk of the X-ray emission comes from hot polar regions, where the temperature is non-uniform, decreasing with distance away from the pole (Zavlin & Pavlov 1998; Zavlin et al. 2002).

For the WD companion, Danziger et al. (1993) give blackbody (BB) fit of $T \sim 4000$ K to ground-based broadband photometry. With such a cool WD, its emission no longer dominates in the UV if the neutron star (NS) is hot enough. This offers a unique opportunity to observe thermal emission from the bulk of the neutron star surface in the UV/optical.

Kargaltsev et al. (2004, hereafter K04) observed PSR J0437−4715 for the first time in the UV with the Space Telescope Imaging Spectrometer (STIS) aboard *Hubble Space Telescope* (*HST*). K04 found a spectrum consistent with the Rayleigh–Jeans tail of thermal emission although the measured spectral shape had a large uncertainty. Assuming the maximum area that this could be emitted from is the surface of the neutron star, they derived a surface temperature of $T \sim 10^5$ K.

Here we describe an extensive observational campaign of PSR J0437−4715 in various spectral bands. In Section 2, we describe the data and its analysis, one spectral window at a time.

---

[8] Rate of loss of rotational kinetic energy $\dot{E} = I\Omega\dot{\Omega}$, for a standard neutron star moment of inertia $I = 10^{45}$ g cm^2.

Table 1
Log of Observations of PSR J0437−4715

Waveband	Observatory/Instrument	Date	Type	Section
Mid-IR	*Spitzer*/MIPS	2005 Sep	Phot	2.1.2
Mid-IR	*Spitzer*/IRAC	2004 Nov	Phot	2.1.1
Near-IR	Magellan/PANIC	2005 Oct	Phot	2.2
Optical	VLT/FORS1	1999 Jul	Spec	2.2
Optical	*HST*/WFPC2	1996 May	Phot	2.4.1
Op/UV	*HST*/ACS	2006 Apr	Phot	2.4.2
NUV	*HST*/ACS	2006 Apr	Spec	2.4.3
FUV	*HST*/ACS	2006 May	Spec	2.4.4
X-ray	*XMM*/E-MOS	2002 Oct	ImSpec[a]	2.5.1
X-ray	*Chandra*/ACIS	Various	ImSpec[a]	2.5.2
Gamma	*Fermi*/LAT	2008–2010	ImSpec[a]	2.6

Note. [a] Imaging on a detector with intrinsic energy resolution.

The results and spectral fits from each data set are presented in Section 3, with a complete multi-wavelength analysis in Section 4. The results are discussed in Section 5, followed by a brief summary and outlook in Section 6.

2. OBSERVATIONS AND ANALYSIS

We utilize a suite of observations of PSR J0437−4715 from ground- and space-based observatories. Here we describe in detail each part of our campaign, and the quality of the resulting data. We obtain spectral data in the mid-IR to γ-rays, with a combination of spectroscopic and imaging photometry observations (see Table 1). We made use of Advanced Camera for Surveys (ACS) on *HST*, FORS1 on Very Large Telescope (VLT)/UT1 of ESO/Paranal, and Persson's Auxiliary Nasmyth Infrared Camera (PANIC) on Magellan I. Furthermore, we have re-analyzed archival *Chandra*, *XMM-Newton*, *Spitzer*, and *Fermi* data. The only measurements already in the literature which we have included (without reanalysis) are the ground-based photometric points of Danziger et al. (1993) and the STIS FUV fluxes of K04.

2.1. Spitzer Mid-IR Photometry

There are archival Infrared Array Camera (IRAC) and MIPS *Spitzer* observations of PSR J0437−4715. The observations in the four *Spitzer* IRAC channels, $3.6\,\mu$m, $4.5\,\mu$m, $5.8\,\mu$m, and $8.0\,\mu$m (Fazio et al. 2004), were carried out in 2004 November, the MIPS $24\,\mu$m observations (Rieke et al. 2004) were done in 2005 September. The pointing accuracy of *Spitzer* is reported to be better than $0\farcs5$, according to the IRAC instrument handbook.[9] Astrometric accuracy of better than $0\farcs2$ can be reached, especially if cross-correlating with Two Micron All Sky Survey (2MASS) point sources is successful. This is the case for the observations of PSR J0437−4715, where around 20 2MASS point sources with IRAC counterparts are in the field. We apply the *Spitzer* Software, MOPEX (version 18.3.3),[10] and its point source extraction package, APEX, for the data reduction, which we describe in detail.

2.1.1. IRAC Observations

The IRAC observations are strongly affected by extended emission, which turns out to be an extended artifact in the detector, probably latent from previous observations. We select only those Corrected Basic Calibrated Data files (CBCD; they already include some pipeline processing) from the dithered observations where the target position is well separated from the artifact. This reduces the depth of the observations; in the case of the fourth channel ($8\,\mu$m), for example, only half of the available coverage can be used. For this channel we removed one more CBCD file because of a cosmic ray hit right at the target position. The resulting mosaics at the target position are shown in Figure 1; for the first channel the position at the epoch of the IRAC observation of PSR J0437−4715 is indicated.

Spitzer IRAC photometric accuracy can reach 2% for *bright* sources, provided the proper aperture correction, the correction of the photometry array location effect, and the color correction are taken into account (Reach et al. 2005). As recommended by the *Spitzer* Science Center, we use aperture photometry instead of profile fitting photometry for the measurements, using a source aperture radius of 2 native IRAC pixels ($1\farcs2$ pixel size) and a sky annulus from 2 to 6 native IRAC pixels to avoid bright sources in the neighborhood. (This results in a slight overestimation of the sky due to flux from the source in the sky aperture. For the bright background and close neighboring sources, the effect is small compared to the photometric uncertainties.) We use the "mode" algorithm for the background estimation in the annulus to limit the influence of a faint neighbor covering part of the annulus. The APEX source extraction clearly detects a source at the target position in IRAC channels 1 and 2, the source is marginally detected in channel 3, and not detected in channel 4. The following flux values for channels 1–3 are aperture corrected as well as corrected for the position-dependent sensitivity, following the IRAC data handbook recommendations: $16.0 \pm 0.4\,\mu$Jy; $11.4 \pm 0.7\,\mu$Jy; and $8.2 \pm 2.5\,\mu$Jy for channels 1, 2, and 3, respectively, where uncertainties are at the 1σ level. The color correction for a 4000–5000 K BB is 1% or less for each channel, so we neglect this.

The choice of the aperture and annulus size has been optimized to include as few neighboring stars as possible. At larger separations from the target additional constraints for background estimates are the remaining artifacts and the varying IR background (we found background differences of up to a factor of three). For IRAC channel 1 we used apertures and annuli of the same size at three different positions in the immediate vicinity of the target to check for conspicuous deviations in the estimated background or noise estimates. The obtained background and noise values are comparable to those of the target measurements. Therefore, we deduce that our aperture and annulus choice is acceptable with no expected significant systematic effects regarding the background or noise estimates. For the longer wavelengths, the variation in the IR background is expected to be even higher.

In IRAC channels 1 and 2 there is a neighboring source close to the target. This source is not seen in channel 3 or 4. The applied apertures for the target as well as for this other source are shown in Figure 1; in case of channel 3 or 4 no aperture measurements of the neighbor source were required, and the dashed circles are only plotted to indicate its position. The APEX source extraction detects the source only in channel 2; we use this position to do aperture photometry in channel 1 as well. The flux density of the neighbor source in channel 2 is $8.5 \pm 1.0\,\mu$Jy and for channel 1 is $6.2 \pm 1.2\,\mu$Jy (1σ confidence).

Roughly 1/3 of the neighbor aperture area is also covered by the target aperture. If the apparent neighbor were a real source, the flux of our target would be the measured value minus

---
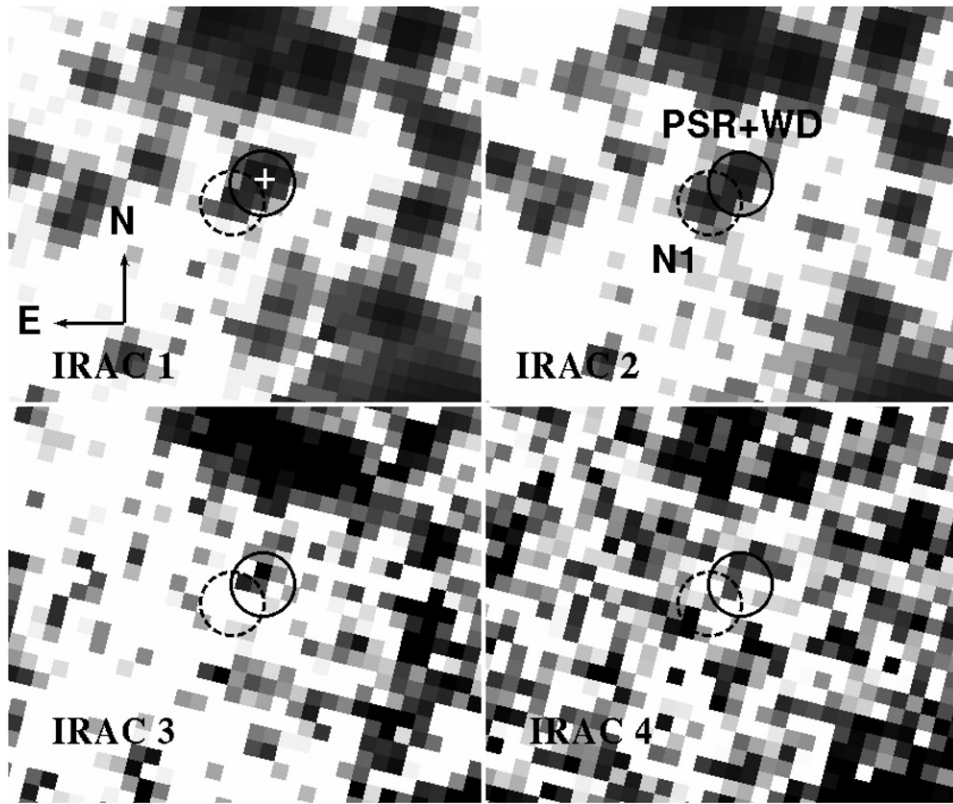
[9] http://ssc.spitzer.caltech.edu/irac/iracinstrumenthandbook
[10] http://ssc.spitzer.caltech.edu/postbcd/mopex.html

Figure 1. IRAC images of the field of J0437−4715 in four channels. The images are $36'' \times 30''$ in size. The VLBI radio position of PSR J0437−4715 obtained by Deller et al. (2008), and corrected for the proper motion to the epoch of the *Spitzer* IRAC observations, is marked by a white cross in IRAC channel 1. The solid circle indicates the aperture (radius of 2 native IRAC pixels) used for the flux density measurements. The dashed circle corresponds to the aperture measurement done for the neighboring source N1 in channel 2. The same position and aperture was also used for channel 1 (see the text), while in channels 3 and 4 N1 is not seen.

the neighbor's contribution; if it were instead some manner of leakage, the target flux would be the sum of both fluxes. As we do not know which of the two options takes place, we leave the flux unchanged, and increase the uncertainty by 1/3 of the apparent neighbor flux. Thus, the target flux density in channel 2 is $11.4 \pm 3.3\,\mu$Jy. Following the same argument as for channel 2, the target flux density in channel 1 is $16.0 \pm 2.7\,\mu$Jy.

We note that the neighboring source is not seen in any of our other observations (X-ray to NIR). The 3σ K_s-band limit is 20.7 mag (see below), indicating an emission maximum at IRAC wavelengths for this object. We suspect, therefore, that it is not a physical source.[11]

The target is not detected in channel 4. We use the source position from IRAC channel 1 for aperture photometry in order to obtain an upper limit for channel 4. We derive a 3σ limit of $22.6\,\mu$Jy on the source flux.

2.1.2. MIPS 24 μm Observations

The photometric properties of MIPS 24 μm observations were reported to be excellent with achievable rms errors of 2% and an accuracy of the absolute calibration being better than 5% (Rieke et al. 2004; MIPS instrument handbook[12]). The pipeline processed PBCD (post-BCD) 24 μm mosaic of PSR J0437−4715 does not show any obvious artifact at the position of the target. As a check, we self-calibrated the data by dividing each EBCD (enhanced BCD) image with a normalized

flat field created by taking the median of all the EBCDs. Self-calibration in this way removes large-scale sky variations and some artifacts. In our case, self-calibration did not improve the data, and we use the unchanged PBCD mosaic from the *Spitzer* pipeline (version: S18.12.0) for our analysis. At the position of the target there seems to be slightly increased count rate; however, it is close to the noise level. We use MOPEX multi-frame point response function fitting photometry and check our chosen parameters by producing a residual image. While we obtain a very good residual image with all prominent sources subtracted well, the source detection algorithm does not find a source at the target position even for very low detection thresholds (2σ). Therefore, we apply aperture photometry at the position of the target as derived from IRAC channel 1. The MIPS 24 μm astrometry generally agrees well with the IRAC astrometry and sources of IRAC channel 2 are overplotted in Figure 2 to illustrate this. For the aperture photometry we use a small source aperture ($3''.5$) and sky annulus ($6''$–$8''$) to avoid close-by bright neighbors. We note that the aperture correction itself has an uncertainty of around 5%, according to the MIPS instrument handbook. The "mode" algorithm for the background estimation in the annulus is employed. We derive an aperture-corrected flux density of $38 \pm 22\,\mu$Jy (1σ confidence) or 3σ upper limit of $105\,\mu$Jy.

2.2. Magellan NIR Photometry

We observed PSR J0437−4715 with PANIC (Martini et al. 2004) on 2005 October 20 with the 6.5 m Magellan I (Baade) telescope. The conditions were close to photometric, with seeing of about $0''.5$. We used exposure times of 18×30 s (K_s band), 9×20 s (H band), and 9×30 s (J band), taken with small

---

[11] In principle, we might have detected an asteroid, but the high latitude and unusual spectral energy distribution (Trilling et al. 2008) argue against this.
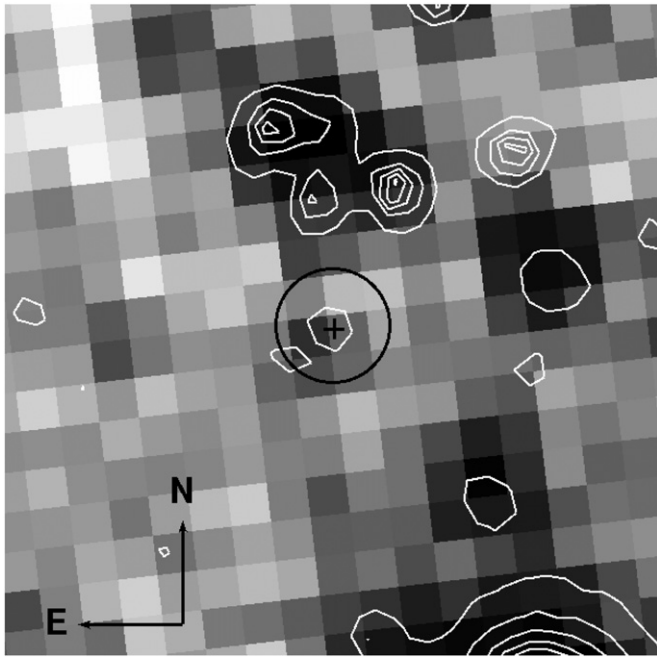[12] http://ssc.spitzer.caltech.edu/mips/mipsinstrumenthandbook

Figure 2. MIPS 24 μm mosaic for the position of PSR J0437−4715. The image covers $40'' \times 40''$. The VLBI radio position of PSR J0437−4715 obtained by Deller et al. (2008) and corrected for the proper motion to the epoch of the *Spitzer* observations is plotted as a black cross. The used aperture ($r = 3''\!.5$) is also shown, together with illustrative overlay contours of the IRAC channel 2 mosaic. The small white contour southeast of the target marks the position where the faint neighboring source is seen in IRAC 1 and 2.

pointing dithers between the exposures. Data reduction followed standard procedures: we masked bad pixels, subtracted dark frames, and flat fielded using well-exposed twilight flats. Sky subtraction was done using a median-combined image of the data. We then combined the individual exposures together, identified the visible stars, and masked them for a second round of sky subtraction. We then made a final mosaic of the individual exposures, see Figure 3.

We calibrated the photometry relative to 2MASS. However, there were not a sufficient number of unsaturated stars in the field of PSR J0437−4715 to do this in one step. We therefore used other fields observed on the same night over a range of airmasses, generally below 1.2. Using only stars that were still in the linear regime of the detector and were not crowded (1–6 stars in each field over five fields), we used aperture photometry in IRAF with a large aperture of $1''\!.9$ radius and a sky annulus from $2''\!.5$ to $3''\!.8$. We corrected to airmass of 1.0 using approximate airmass coefficients for the site (0.10, 0.03, and 0.07 mag airmass^{-1} for J, H, and K_s, respectively) and determined the zero points for the night. The final photometry for PSR J0437−4715 is $J = 18.59 \pm 0.02$, $H = 18.37 \pm 0.06$, and $K_s = 18.38 \pm 0.06$, where the errors are statistical only. We estimate that the uncertainties in the photometric zero points were at most 0.03 mag for K_s and H, and 0.02 for J.

2.3. Optical Spectroscopy

Spectra of the optical counterpart to PSR J0437−4715 were taken on the night of 1999 July 15 using FORS1 at the VLT. The
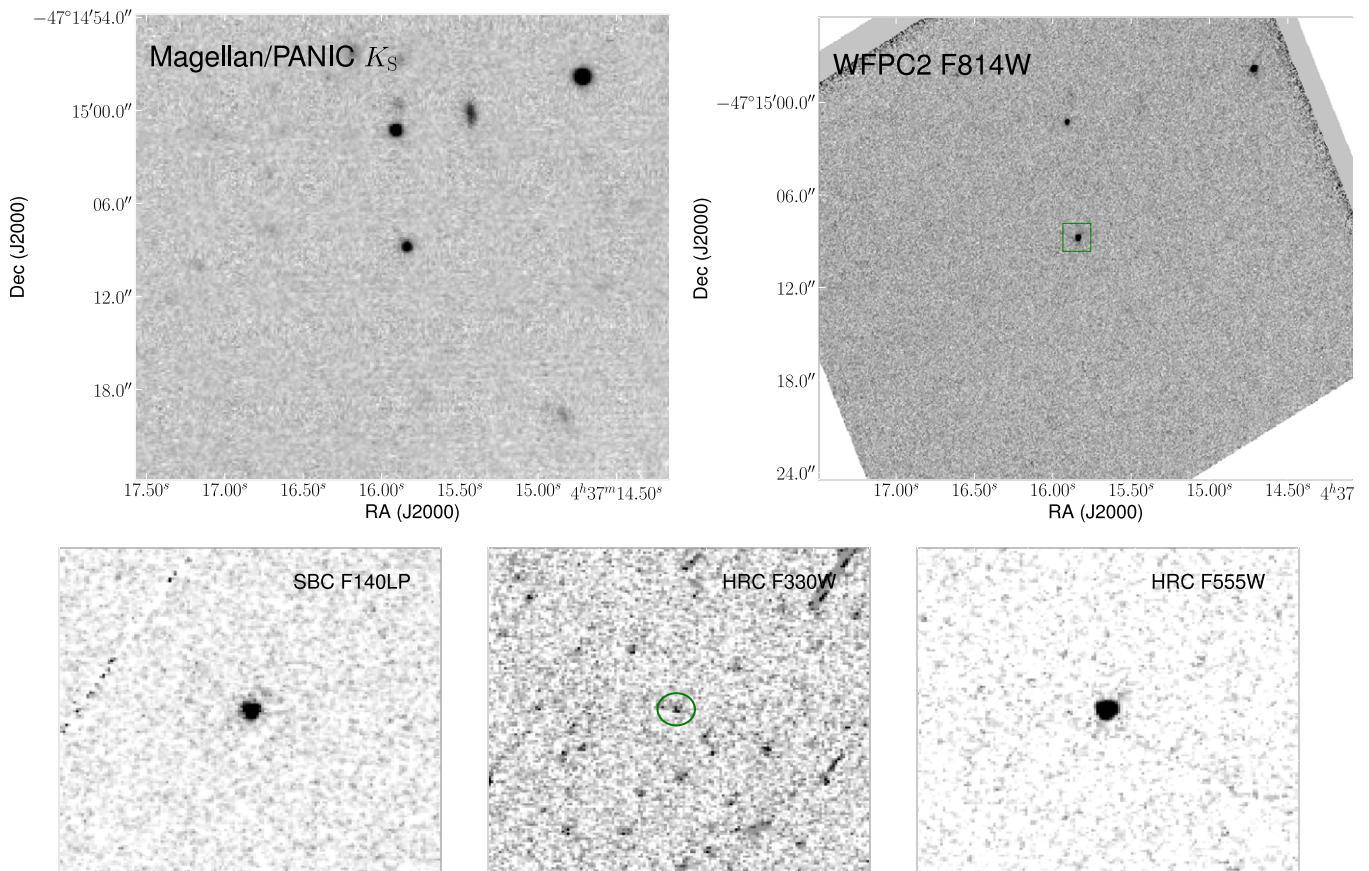

Figure 3. Broadband imaging of PSR J0437−4715; north is up. In each case, the source is in the center of the image. Note the cosmic rays affecting F330W (because this was a single exposure, see the text; we have masked cosmic rays). No counterpart of the faint IRAC neighbor of PSR J0437−4715 (Figure 1) is seen in the K_S-band image. The field of the ACS images is shown on the F814W image.

setup was the same as that used by van Kerkwijk & Kulkarni (2001) for a spectroscopic study of the faint neutron star, RX J1856.5−3754 (Grism 300V with $R \approx 300$, 2.6 Å pixel^{-1} dispersion; 1″ wide long-slit, 0″2 pixel^{-1} spatial scale). The reduction followed that described by those authors. Briefly, two 45 minute spectra were taken, covering the range of 3600–9000 Å at a resolution of ∼13 Å, with the slit position angle chosen such that both the counterpart and star 1 of Bailyn (1993) were covered.[13] The reduction involved bias subtraction, sky subtraction, and optimal extraction (Horne 1986) of the spectra of the counterpart using the spatial profile of star 1.

Flux calibration was done in two steps. First, we calibrated the fluxes of star 1 using a shorter, 5 minute spectrum taken through a wide slit (with the instrumental response determined from two flux standards; see van Kerkwijk & Kulkarni 2001, especially their Section 4.4). Next, we estimated the slit losses by fitting a quadratic function to the ratio of the narrow-slit to wide-slit spectra of star 1 and used this to calibrate the fluxes of the counterpart. Overall, we believe our relative fluxes should be accurate to about 5% between 4500 and 8800 Å. Shortward of 4500 Å, the calibration is more uncertain, since it is less clear whether our slit losses are corrected well: the ratio of the narrow-to wide-slit spectra of star 1 shows systematic, ∼10% deviations, likely because the wide-slit spectra were taken at high airmass. The absolute flux calibration is also less certain, since there was some cirrus at the start of the night. We find that we have to scale the fluxes up by 8% to match the *HST* photometry in Section 2.4. Furthermore, some regions of the spectrum are contaminated by atmospheric absorption and high background—we have simply excluded these areas from consideration.

2.4. HST

We analyzed several observations of PSR J0437−4715 with the *HST*, both imaging (WFPC2 and ACS) and spectroscopy (ACS). The ACS observations consisted originally of five visits, one in the NUV and optical using the High-resolution Camera (HRC) and the remainder in the FUV, using the Solar-blind Channel (SBC) detector.

2.4.1. WFPC2 Imaging

We retrieved WFPC2 observations of the field of PSR J0437−4715, taken in the two wide-band filters F555W and F814W (roughly *V* and *I* bands) on 1996 May 19. There were four exposures of 140 s each, for a total of 560 s taken through each filter. The source was located on the PC chip of the array in every case, with a pixel scale of 0″0455 pixel^{-1}. Photometry was performed using HSTphot (Dolphin 2000), a software package optimized to WFPC2 photometry by profile fitting. It efficiently rejects bad data (hot pixels and cosmic ray hits) and fits stellar profiles from libraries of pre-built point-spread function (PSF) images (originally created using TinyTim).

For the source, we obtained (Vega-magnitudes) $m_{F555W} = 20.899(10)$ and $m_{F814W} = 19.416(8)$. Since the observations were taken early in the WFPC2 lifetime, the charge transfer efficiency (CTE) corrections are very small.

2.4.2. ACS Imaging

Imaging observations are required by the prism spectroscopy, as a way to set the wavelength scale for each extracted spectrum. These images are useful, in their own right, for accurate broadband photometry. From our observations, we have three bands, F555W, F330W, and F140LP, each with a detection of the PSR J0437−4715 system. One exposure was acquired in each single orbit, at the start of each orbit for the NUV and the end for the FUV. We performed aperture photometry on these, with an aperture size set to contain about 90% of the flux, which maximizes the signal-to-noise ratio (S/N). The correction to total flux was done using the encircled energy tables in the *ACS Instrument Handbook*[14] (see also Sirianni et al. 2005) and converted to flux using the information supplied in the image headers. These are based on the latest calibration at the time of download (2010 January). Figure 3 shows the fields centered on PSR J0437−4715 in the three broadband filters.

For F555W and F140LP, multiple images could be used to effectively remove cosmic rays and detector blemishes. We only had one F330W image to work with, however, so such rejection was not possible. No cosmic ray is seen in or around the photometry aperture.

The CTE correction for the flux in F555W is very small because the source is comparatively bright in that filter.[15] On the other hand, the F330W flux does have a substantial correction of the order 5%–10%. In this case, the flux is already relatively uncertain (see Table 3), and the CTE effect also increases the uncertainty.

2.4.3. NUV Spectroscopy

For the reduction of all the spectral data, we used the slitless spectroscopy package aXe,[16] Version 2.0 (released on 2009 November), in conjunction with IRAF/PyRAF. A detailed description of the algorithms used by aXe are given in Kümmel et al. (2009). In summary, a spectral observation requires a direct (broadband) image taken with the same pointing, which serves to calibrate the wavelength scale on the subsequent dispersed image. For the tilted spectrum, pixels within an adjustable distance in the orthogonal direction to the trace are summed. The background is determined in a region at large distance either side of the trace.

The derivation of the wavelength solution, sensitivity curve, and aperture correction is detailed in STScI Instrument Science Report (ISR) 0603.[17]

The ACS HRC is sensitive in the wavelength range 1700–10000 Å. For the PR200L prism observations, we used the direct images taken in the F555W filter. Since all the exposures for the NUV were taken during a single visit, they are very well aligned with one another. Although in slitless spectroscopy spectra can in principle overlap, in our case, the source is well isolated and the brightest in the field, so such contamination is not an issue.

Although the individual exposures are the ones used in the analysis, running MULTIDRIZZLE ensures the masking of cosmic rays as bad data, and provides an opportunity to perform visual inspection of the data. Cosmic rays are not removed, but a flag is set in the data quality (DQ) extension of the input image, marking that pixel as unusable. In order to make use of this filtering out of bad data, it is necessary to copy the modified DQ extension into the original, unmodified image file, and use this as input for aXe.

Figure 4 shows the combined spectral image in the vicinity of PSR J0437−4715. A number of interesting features are seen.

---

[13] The star is also known as 086-010575 in UCAC3.

[14] http://www.stsci.edu/hst/acs/documents/handbooks/cycle18/cover.html
[15] www.stsci.edu/hst/acs/documents/isrs/isr0901.pdf
[16] http://www.stecf.org/software/slitless_software/axe/
[17] See http://www.stecf.org/documents/isr/isr0603.pdf

Table 2
Broadband Photometry of PSR J0437−4715

Origin	Band	Central Wavelength[a] (Å)	Bandwidth (Å)	Spectral Flux F_λ (10^{-18} erg s^{-1} cm^{-2} Å^{-1})
HST	F555W	5356	357	15.58(15)
	F330W	3363	174	1.9(2)
	F140LP	1451	127	2.93(9)
Magellan	J	12200	2130	11.6(4)
	H	16300	3070	5.2(4)
	K_S	21900	3900	1.77(12)
Spitzer	IRAC1	35500	7500	0.37(6)
	IRAC2	44900	10150	0.17(5)
	IRAC3	57300	14250	0.07(3)
	IRAC4	78700	29050	<0.22
	MIPS24	240000	91300	0.38(20); <1.05
Danziger et al.	B	4420	940	8.17(16)
	V	5450	880	16.8(10)
	R	6380	1380	21.1(6)
	I	7970	1490	17.9(7)

Note. Numbers in parentheses indicate 1σ statistical uncertainties in the last digit(s).

Table 3
FUV and NUV Spectral Data

Wavelength Bin Center (Å)	Bin Width (Å)	Gross Counts	Background Counts	Net Counts[a]	Flux[a] F_λ (10^{-18} erg s^{-1} cm^{-2} Å^{-1})
1245	30	403	225	178(20)	6.42(0.80)
1275	30	424	177	247(21)	5.34(0.53)
1305	30	412	144	268(20)	5.19(0.48)
1335	30	387	106	281(20)	5.36(0.47)
1365	30	348	93	255(19)	5.00(0.45)
1395	30	256	70	186(16)	3.86(0.39)
1425	30	253	70	183(16)	4.05(0.41)
1455	30	171	51	120(13)	2.86(0.35)
1485	30	188	49	139(14)	3.60(0.40)
1515	30	195	49	146(14)	4.16(0.46)
1545	30	132	39	93(11)	2.99(0.40)
1575	30	128	41	87(11)	3.18(0.45)
1605	30	119	39	80(11)	3.36(0.50)
1645	50	163	55	108(13)	3.27(0.43)
1695	50	107	41	66(10)	2.42(0.41)
1745	50	111	41	70(12)	3.36(0.55)
1795	50	99	41	58(10)	4.26(0.78)
1845	50	53	27	25(7)	3.16(0.94)
2150	700	54808	52685	2123(230)	1.54(0.64)
2600	200	7699	7006	693(88)	1.07(0.15)
2750	100	3053	2648	405(55)	1.27(0.18)
2850	100	3127	2731	396(56)	1.15(0.17)
2950	100	3167	2516	651(56)	1.72(0.17)
3050	100	2177	1689	488(47)	1.17(0.13)
3150	100	2620	1894	726(51)	1.68(0.15)
3300	200	4635	3243	1392(68)	1.73(0.27)
3500	200	4096	2377	1719(64)	2.33(0.36)
3700	200	2506	1203	1303(50)	1.92(0.30)
3900	200	2824	1238	1586(50)	2.54(0.41)

Note. [a] Uncertainties are statistical only for the net counts and include both statistical and systematic/calibration contributions for the flux. Numbers in parentheses show 1σ uncertainties.

The bright elongated source is the area where the dispersion becomes very small, and all the light for wavelengths $\lambda >$ 5000 Å ends up centered on just a few pixels (the red pile-up effect). Since the source is intrinsically red (the cool WD dominates, see Section 3.1.2), this large halo dominates over the faint spectral trace. Faint discrete structures are seen around the bright source, probably associated with reflections within the optical system, and restricted to $\lambda > 4000$ Å. A diffuse halo of greater extent is also seen, possibly the wings of the PSF in the cross-dispersion direction. Not seen by eye, but present in the background analysis, the bright core at pixel (800, 570) also has a diffraction spike along the x-axis, at a small angle to the
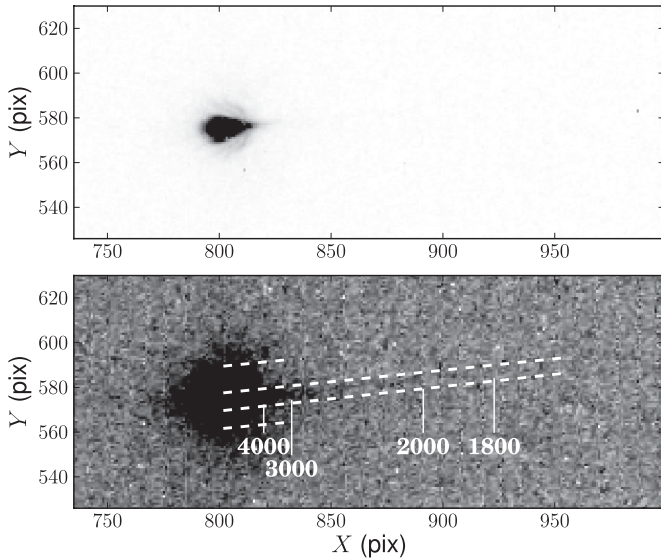
Figure 4. NUV spectral image of PSR J0437−4715 through prism PR200L. Wavelength decreases left to right, nonlinearly, as marked (values in Å). The large source seen at long wavelengths (left) is due to the red pile-up, see the text. The upper panel shows the bright red source caused by the red pile-up, and its surrounding reflection and diffuse structures. The lower panel is the same, but with the color scale stretched, and the extraction regions marked. The background regions used for long wavelengths are also marked; the background regions for short wavelengths lie far from the spectrum (see the text).

Figure 5. FUV combined spectral image of PSR J0437−4715 through prism PR130L, as produced by `multidrizzle`. The extraction region is labeled, along with approximate wavelengths in Å.

spectral trace. This limits the size of extraction region which will be free of contamination, particularly for intrinsically red sources (e.g., Walkowicz et al. 2008).

We calculated final fluxes by heavily binning the count rates measured by aXe, together with the provided sensitivity curve and aperture correction (see ISR 0603[18]).

We find, after much experimentation, that the optimum trade-off between gathering enough signal and gathering too much noise and contamination was at an aperture half-width of $1 \times$ FWHM (7 pixel full width). For the background estimate we employed two regimes: at the faint, short-wavelength end ($\lambda < 3175$ Å), where there was no bright halo, and the diffraction spike would be far from the source, we used a region from $20 \times$ FWHM to $21.5 \times$ FWHM from the trace. For longer wavelengths, where the halo contamination will be significant, we used a background sampled from $1.5 \times$ FWHM to $3 \times$ FWHM from the trace in order to subtract this contribution, but corrected the flux upward for the small amount of source flux ($\approx 6\%$) that will fall in the background sampling region. We also compared the results with those obtained using optimal extraction. In theory, optimal extraction should enhance the S/N if the trace is well sampled in the spacial direction. We found that the optimal extraction produced a smoother spectrum, in better agreement with the broadband photometric point at 3363 Å, so we have reason to believe that it is a fair extraction in this case; we therefore use the optimal extraction fluxes.

The final uncertainties on the fluxes are a combination of Poissonian photon noise (in both the signal and the background), small uncertainties in the sensitivity curve, and larger systematic calibration uncertainties of 5% in the range 1800–3000 Å rising to 15%–20% at the edge of the sensitivity range (M. Kümmel 2010, private communication). All the uncertainties were added in quadrature. The final set of counts and fluxes for the wavelength bins chosen are listed in Table 3.
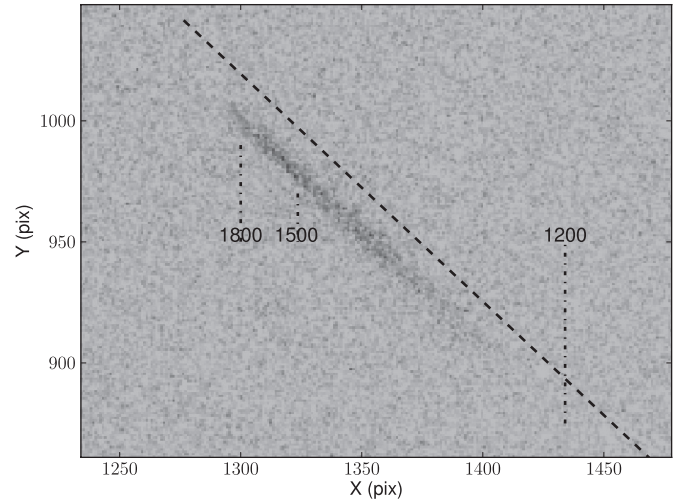
2.4.4. FUV Spectroscopy

PSR J0437−4715 was imaged through the PR130L prism. This prism was chosen in order to decrease the background level, since it has low throughput shortward of 130 nm, and thus limits the contribution of the brightest geocoronal lines. Furthermore, the spectral exposures were taken while the spacecraft was in Earth's shadow, further reducing the background. The imaging exposures were done in the remainder of the orbit. In addition, the SBC's Multi-Anode Microchannel Array detector does not suffer from cosmic ray hits as do CCD detectors. As the resulting combined image in Figure 5 shows, the background is faint and uniform, and the spectrum is very easy to see. In comparison to the NUV observations, the spectral trace is well defined, and there is no background structure or any halo/pile-up effects.

Reduction proceeded in a similar way to the NUV spectral analysis above. Since the exposures come from separate visits in this case, and therefore required re-acquisition of a guide star, alignment between them is not guaranteed, and the source position on the direct image was translated back to each input direct image using the aXe task IOLPREP. This was particularly important for the Visit 02 exposures, because of the loss of the guide star during this visit. The data had an enhanced background level, and the data from the last orbit were totally lost. Nevertheless, we do include the data from the first part of the visit and find that it improves rather than decreases the S/N. Before proceeding with the extraction, the input coordinates need to be corrected for an offset caused by the choice of broadband filter for imaging (see ISR 0602[19]).

Due to the much lower background level compared to the NUV, and the absence of the problems associated with red pile-up and diffraction spikes near the spectral trace, it proved to be optimal to extract the source from a somewhat wider aperture, half-width of $4 \times$ FWHM (19 pixel full width). See Figure 5 for the locations of the extraction region. The results are listed in Table 3. With the low sensitivity, the systematic uncertainties in the calibration make less of an impact in this case, and optimal extraction produced a spectrum that looks a little noisier, but otherwise similar—we therefore used simple

---

[18] See http://www.stecf.org/documents/isr/isr0603.pdf

[19] http://www.stecf.org/documents/isr/isr0602.pdf

fixed aperture extraction. Systematic uncertainties are of the order 5% throughout the spectral band analyzed.

2.5. X-Rays

We retrieved one long *XMM-Newton* observation and nine *Chandra* observations from the archives, and re-processed all the data to be analyzed simultaneously. The data consist of CCD imaging and provide low-resolution spectra using the inherent energy resolution of the detector, as opposed to inserting a spectral element such as a grating. Although the Reflection Grating Spectrometer instrument of *XMM-Newton* does provide such data, its count rate was too low for consideration.

2.5.1. XMM-Newton

XMM-Newton observed PSR J0437−4715 on 2002 October 9, 03:32:34–22:50:04. This observation and its analysis are described in detail by Zavlin (2006). Here we consider the data from the two EPIC-MOS detectors, operated in Full Window mode (2.6 s time resolution) and the EPIC-PN detector operated in Fast Timing mode (0.03 ms time resolution). The raw data were processed into calibrated event files using the standard tasks of the provided software XMM-SAS, version 9.0 (20090615_1801). After filtering the data for times of flaring, the total live time was 63.0 ks for the MOSs and 62.9 ks for the PN.

For the MOS data sets, we extracted the source spectrum from a circle of 15″ radius centered on the source. This only captures some 70% of the total flux, but such a compromise is necessary because of the relatively high background and the background from a circular annulus with inner and outer radii of 114″ and 200″, respectively.

In timing mode, all information about the Y-axis position of a photon on the detector is lost. We filtered out low-energy electronic noise[20] by keeping only energies $E > 600$ eV. There is a bright active galactic nucleus (AGN) in the field whose one-dimensional PSF partly overlaps with that of the pulsar (see Zavlin et al. 2002). We therefore extracted counts from an aperture chosen to avoid contamination that only contained 61%–66% of the flux (higher fraction for lower energies). We correct the spectrum for this finite-aperture effect.

2.5.2. Chandra

We retrieved nine *Chandra* ACIS imaging data sets, with IDs 6154, 6157, 6767, 6768, 741, for a total exposure time of 73.2 ks. We do not consider HRC observations nor ACIS observations affected by pile-up. The observations have a range of exposure times and off-axis distances. The total exposure time was 73.2 ks.

The source extraction region was chosen to be fairly large and uniform for all the observations, as the background is low, and the varying off-axis distance for each observation means the size of the PSF is different. The radius was set at 9.15 pixel (4″.5), which includes some 99% of the flux for the on-axis PSF, and most (≈90%) even for the broadest PSF in the set of observation. The background was taken either from an annular region centered on the source, or rectangular regions either side of the readout direction, for observations with subarrays, where the active area is restricted in one direction.

---

[20] http://www.star.le.ac.uk/∼amr30/BG/BGTable.html, column titled Electronic Noise

2.6. Fermi

We retrieved data on the region containing PSR J0437−4715 collected in 18 months of *Fermi* Large Area Telescope (LAT) observation. γ-ray data have much lower count rates than X-rays, extended, broad-winged PSF, and frequency-dependent energy resolution. Standard filtering (see Abdo et al. 2010) was applied. The reduction to obtain a spectral model or fluxes for a single source is therefore a likelihood maximization method, with explicit consideration of nearby sources and their respective spectra. Since spectral fitting is then an intrinsic part of the extraction process, we describe it in Section 3.3.

3. SPECTRUM AND FITS

In Figure 6, we show the UV–IR spectrum of J0437. Note that we do not include the MIPS point, since it is more likely to be a (non-restrictive) upper limit. It is reassuring to see the high degree of agreement between our FUV spectral points, the F130LP broadband photometry, and the previous STIS spectrum. Likewise, the NUV spectrum and the F330W photometry agree, but there is no independent data in this region to verify the spectral shape. Furthermore, the NUV and optical points support a smooth continuum linking the two spectral regions. Given the several problems inherent in processing the PR200L data, we regard with suspicion the hint of structure around 3700 Å.

The extinction to the source is not well constrained by fits to the X-ray spectrum, but must be small, with the hydrogen column of $\sim 10^{20}$ cm^{-2} or less (Zavlin et al. 2002). This is equivalent to $E(B - V) < 0.05$, consistent with the small distance to the source, $d = 156.3$ pc. We therefore attempt to model our combined spectrum with extinction values $E(B - V) = 0.01$, 0.03, and 0.05. Furthermore, there is some considerable difference in the extinction curves in the literature, for a given value of extinction. This is an additional uncertainty in our fits. In practice, the shapes of the extinction curves in, for instance, Seaton (1979) and Cardelli et al. (1989) are very similar, but different in normalization. We will use Cardelli et al.'s (1989) more recent parameterization for our fitting.

In the NUV and FUV, we considered only the spectroscopic fluxes because of the lower S/N of the F330W point and the extreme asymmetry of the F130LP bandpass.

3.1. UV to Mid-IR

3.1.1. Analytic Models

We first fit the observed spectrum with simple analytical models. In particular, the maximum in the optical can be fitted with a BB curve, and the FUV–NUV with a PL ($F_\lambda \propto \lambda^\alpha$; PL). We attempt this for different reasonable values of reddening, $E(B - V) = 0.01$, 0.03, 0.05. The results of these fits are shown in Table 4. It should be noted that none of these fits is statistically acceptable (see Figure 7), but the numbers can be taken as indicative. The spectrum shortward of 1500 Å appears to be well represented by the $\alpha \approx -3.5$ PL.

We can see that a simplistic sum of a ~ 4000 K BB and a PL with $\alpha = -(3-4)$ (i.e., close to a Rayleigh–Jeans tail of a thermal spectrum with a high temperature) roughly describes the data. The apparent BB emitting radius is about 20,000 km (or 0.028 $R_\odot$).

3.1.2. WD Atmosphere

Although informative, the BB only crudely approximates the optical–IR spectrum above and cannot reveal information on
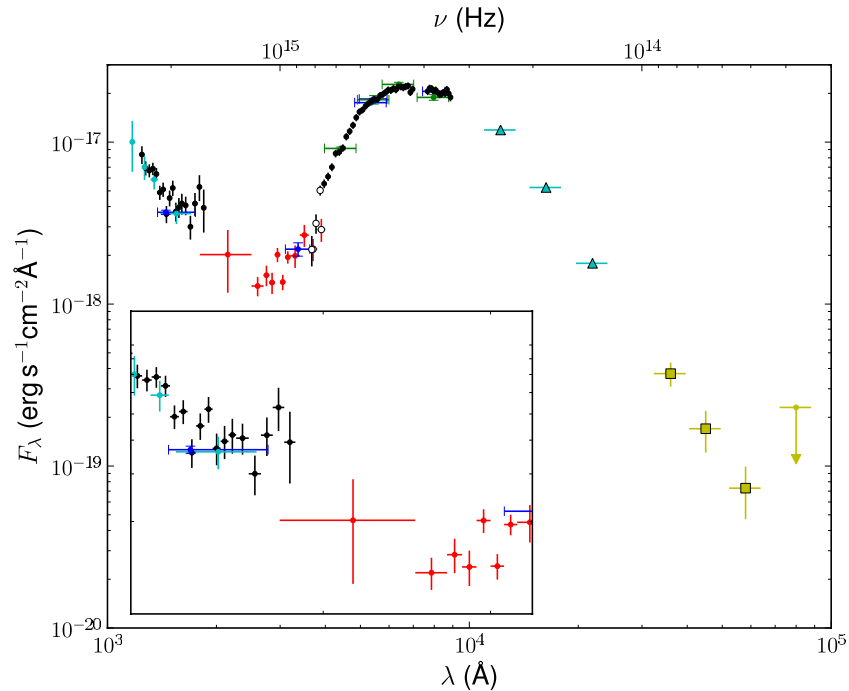
Figure 6. UV to mid-IR spectrum of PSR J0437−4715 with a zoom of the UV portion in the inset. Black points are from prism PR130L (UV) and VLT/FORS1 (optical), red points from prism PR200L, blue points from *HST* broadband imaging, cyan triangles from Magellan/PANIC IR photometry, and yellow squares (and a limit) from *Spitzer* photometry. Cyan UV points are from previous STIS spectroscopy (K04), and green points are ground-based photometry from Danziger et al. (1993). Open markers denote fluxes from FORS1 or PR200L with uncertain calibration.

(A color version of this figure is available in the online journal.)

Table 4
Fits to IR–UV Spectrum

$E(B-V)$	T (K)	R^{a}	α	N_{PL}^{b}
		BB+PL		
0.01	3870(40)	2.02(11)	−3.3(4)	3.7(2)
0.03	3910(40)	1.97(11)	−3.4(4)	4.3(3)
0.05	3950(40)	1.95(11)	−3.5(4)	5.0(3)
		WDA+PL		
0.03	3950(150)	1.87(20)	−2.46(17)	4.61(19)

Notes. Blackbody plus power-law fits (Section 3.1.1) and WD atmosphere model plus power-law fit (Section 3.1.2). Uncertainties are 1σ, taken from the diagonal of the covariance matrix and assuming the fit is reasonable.
[a] Effective radius for a distance of 156.3 pc, units of 10^4 km.
[b] Spectral flux of the PL component at 1500 Å, in 10^{-18} erg s^{-1} cm^{-2} Å^{-1}.

the surface properties of the WD. A better description could be provided by a detailed WD atmosphere model. Atmosphere models have been developed for a variety of WD masses, ages, and compositions (e.g., Bergeron et al. 1995). Note that, in principle, the WD surface is irradiated by the higher-energy emission of the companion pulsar, but the effect is small: for the known binary separation (Verbiest et al. 2008), the radiative intensity from the pulsar (see also Section 4) at the distance of the WD is approximately 3×10^8 erg s^{-1} cm^{-2}, about 2% of the outward radiative flux; we therefore neglect it in our modeling. We describe in detail the model fitting process.

The spectrum of the WD companion was modeled using white dwarf atmosphere (WDA) models that account for recently introduced improvements in the description of the atmosphere of these stars, especially Lyα absorption in the UV (Kowalski & Saumon 2006), opacity of helium-dominated medium (Kowalski 2006; Kowalski et al. 2007), and refraction (Kowalski

& Saumon 2004). The models used in the analysis were successful in describing the entire spectral energy distributions of many cool WDs, including the UV spectrum of pure-H atmosphere WD BPM 4729 (Kowalski & Saumon 2006) and the near-UV spectra of WDs with $T_{eff} \sim 4000$ K (Kilic et al. 2010).

The fit in effective temperature and gravity for He and H atmospheres was performed for the known photometry, *BVRI* of Danziger et al. (1993), and Magellan *JHK* and *Spitzer* IR measurements reported here, assuming that the distance to the system is 156.3 pc (Deller et al. 2008) and the reddening is $E(B-V) = 0.03$. The spectral energy distribution of the WD is best reproduced by a pure hydrogen atmosphere model. The hydrogen is clearly visible, when comparing with pure-He model spectrum, by strong absorption in the UV, due to strong Lyα red wing opacity (Kowalski & Saumon 2006) and flux suppression in the IR due to collision-induced absorption (CIA) by molecular hydrogen (Saumon & Jacobson 1999). The best-fit model closely matches the VLT/FORS1 spectrum (see Figure 7).

The best-fit effective temperature, $T = 3950 \pm 150$ K, is in agreement with previous estimates (Bell et al. 1993; Bassa et al. 2006; Danziger et al. 1993) and the BB fit from above, see Figure 7. The obtained gravity ($\log g = 6.98 \pm 0.15$ [cgs]) fits the models of a helium core WD (Sarna et al. 2001; Althaus et al. 2009), assuming the mass of the companion to be 0.254 $M_\odot$ (Verbiest et al. 2008). The uncertainties are estimated from the uncertainty in the photometric fluxes (Table 2), and the small uncertainties in the distance and WD mass. We include the fit parameters in Table 4; we also list the radius, R, which is fitted implicitly via $\log g$ (because the mass is well known); the quoted error reflects uncertainties in the temperature and distance. Without spectral lines, the spectrum provides no distance-independent constraints on the gravity.
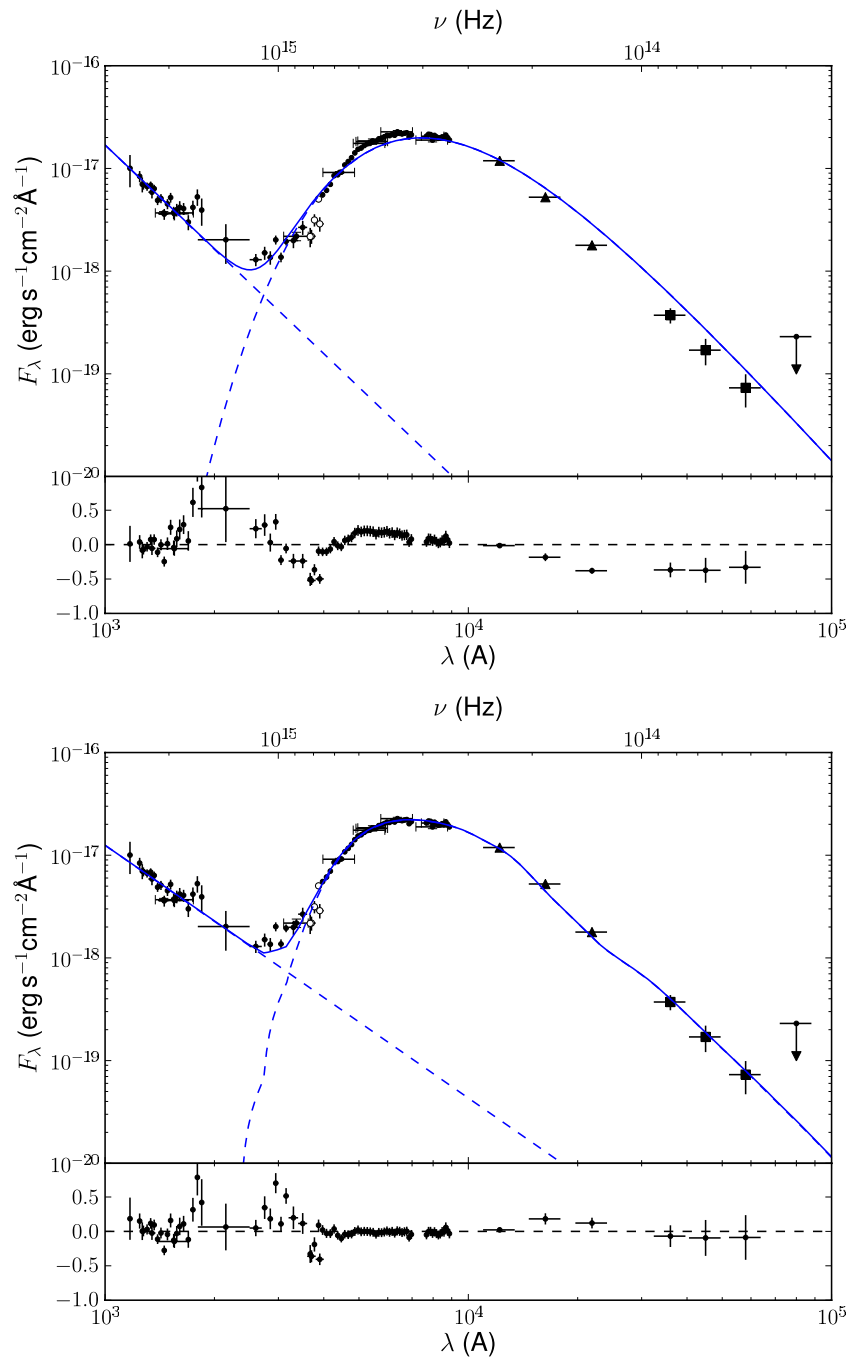
Figure 7. Top: blackbody plus power-law fit to the spectral data for PSR J0437−4715. This is the case for the preferred value of reddening $E(B − V) = 0.03$, giving $T_{BB} = 3910$ K, $\alpha = −3.4$. The lower panel shows fractional residuals (flux-model)/model. Bottom: model with white dwarf atmosphere ($T_{eff} = 3950$ K, log $g = 6.98$, pure H) and power law, with index $\alpha = −2.46$ (solid blue). The two components are shown separately (dashed blue). The lower panels show fractional residuals: (flux-model)/model.

(A color version of this figure is available in the online journal.)

While some of the cool WD pulsar companions have optical photometry, this is usually not enough for definitive assignment of their atmospheric chemical composition and parameters (see discussion in Bassa et al. 2006). At so low temperatures the admixture of helium should produce substantially different CIA effect due to H_2–He collisions and therefore would be different from pure hydrogen atmosphere spectrum in the IR, as indicated in Figure 5 of Hall et al. (2008). In this study we present the full spectral energy distribution of the companion, and by obtaining good match with the pure-H atmosphere model we can be

confident that the object is indeed an H-atmosphere WD. This allows for proper derivation of the atmosphere parameters (T_{eff}, g) and the age of the WD. Measurements of near- and mid-IR fluxes are essential for a definitive assignment of the atmosphere composition of other cool WD pulsar companions. The WD companion atmosphere of PSR J0751+1807 was classified as helium-rich by Bassa et al. (2006), which is at odds with the evolutionary models for such stars. In that particular work such a conclusion was reached by performing analysis with the WD atmosphere models of Bergeron et al. (1995). However, these
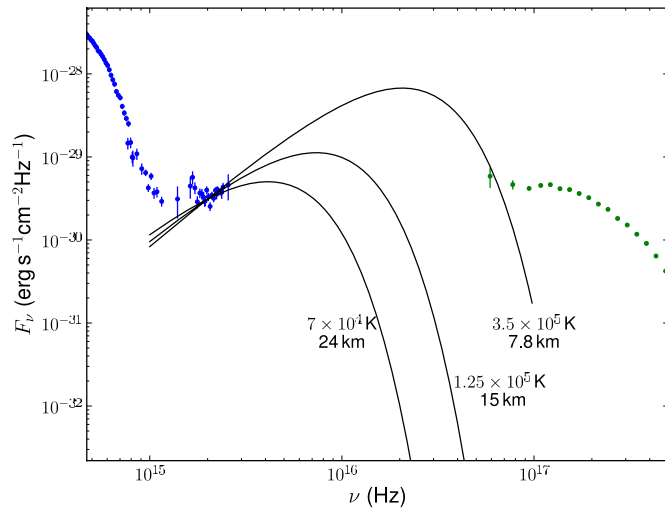
Figure 8. Thermal fits to the de-reddened FUV spectrum (points and error bars, left), showing the coolest temperature allowed by the data ($T = 7 \times 10^4$ K) but with a radius too large for an NS; the coolest temperature compatible with an NS-sized emitter of $R = 15$ km, $T = 1.25 \times 10^5$ K; and the hottest temperature allowed by the X-ray data (extinction-corrected points and error bars, right), $T = 3.5 \times 10^6$ K with an emitting radius of 7.8 km. These values correspond to UV reddening $E(B - V) = 0.03$ and X-ray extincting column $N_H = 7 \times 10^{19}$ cm^{-2}.

(A color version of this figure is available in the online journal.)

models tend to bias the prediction of the atmospheric content of a cool WD from hydrogen-rich to helium-rich, as they do not fully account for the red wing of the Lyα absorption and the free–free opacity of dense helium (see discussion in Kowalski & Saumon 2006). Our conclusion for the atmospheric composition of WD companion of J0437−4715, obtained by a good fit to the entire WD spectral energy distribution by the pure-H atmosphere model, is in line with other works, which postulate a pure hydrogen outermost layer (Hansen & Phinney 1998; Sarna et al. 2001).

Using this (now fixed) model for the WD spectrum, we can again fit a PL to the pulsar part of the spectrum. We choose to fit the range $\lambda < 3575$ Å, where the pulsar dominates. The fit is to be compared with the BB fits in Table 4; we find $\alpha = -2.46(17)$, $N_{PL} = 4.61(19) \times 10^{-18}$ erg s^{-1} cm^{-2} Å^{-1}. From Figure 7, it would appear that the fit is good, except for the portion of the spectrum in the NUV, where the WD atmosphere and the PL are of similar strengths. Also, the value of the PL index is somewhat puzzling, since it is no longer thermal-like, nor is it typical for a pulsar non-thermal spectrum. Indeed, the residuals in the FUV appear to show a systematic slope. This suggests that the UV spectrum may actually consist of two components, for instance, a thermal Rayleigh–Jeans tail (PL with $\alpha = -4$) and a non-thermal PL more typical of old MSPs (PL with $-1 \geqslant \alpha \geqslant -2$, i.e., photon index $1 \leqslant \Gamma \leqslant 2$)—see Section 4.

3.1.3. Thermal FUV

Using *HST*/STIS, K04 were able to measure the FUV spectrum in four bins with low S/N, which rendered the measurement of the spectral slope rather uncertain. Our much better quality FUV spectrum from ACS matches those STIS fluxes rather well (Figure 6) and also the FUV broadband photometry. This gives us confidence in the accuracy of the cross-calibration between the instruments.

Under the assumption that the FUV PL-like emission is indeed a Rayleigh–Jeans law ($F_\lambda \propto \lambda^{-4}$ or $F_\nu \propto \nu^2$), we
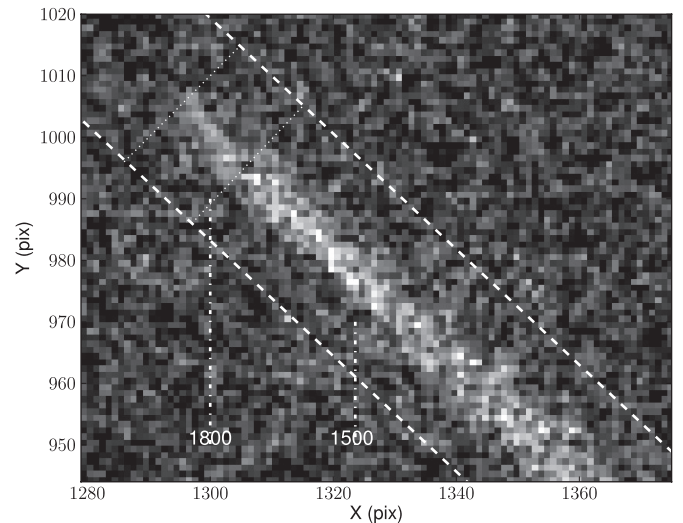

Figure 9. Image of the PR130L spectrum in the region of the possible line at 1800 Å. The approximate extent of the feature is marked by white dotted lines.

can constrain the temperature and radius of the emitting body for the known distance, $d = 156.3$ pc. We calculate $TR^2 = 1.9 \times 10^7$ K km^2. In the case here, however, a BB law starts to deviate from a Rayleigh–Jeans law in the FUV for temperatures $T < 5 \times 10^5$ K. Note that $R \equiv R_\infty$ and $T \equiv T_\infty$, i.e., the temperature and radius as measured by a distant observer.

We show possible thermal fits to the FUV spectrum in Figure 8. We include the lowest-energy points from the X-ray spectra in Section 3.2—these constrain the high-temperature limit of the possible thermal emission to $T \leqslant 3.5 \times 10^6$ K. The lower limit on the temperature is set by requiring that the emitting area be reasonable for an NS. Whereas temperatures as low as 7×10^4 K can still roughly fit the data, the required radius, 24 km, is larger than the largest plausible value of 15 km (Lattimer 2010). For $R = 15$ km, the corresponding surface temperature is $T = 1.25 \times 10^5$ K, and the likely NS size of $R = 13$ km yields a surface temperature of 1.5×10^5 K.

All of these estimates are affected by the choice of reddening in the FUV and extinction in X-rays (for the upper limit). All the temperatures quoted are for $E(B - V) = 0.03$ and should be corrected upward or downward by about 15% for $E(B - V) = 0.05$ and $E(B - V) = 0.01$, respectively. Similar to the WDA+PL model in the previous section, any WDA+thermal model leaves noticeable residuals in the NUV range (see Figure 7).

3.1.4. Emission Line?

In Figure 7, enhanced flux seen in the residuals around 1800 Å, attributable to three bins of the FUV spectrum. Figure 9 shows a zoom of the combined spectrum image, with enhanced contrast, and the vicinity of the line marked. No feature is seen in the raw data by eye; the spectral response is, however, rapidly falling to longer wavelengths in this region. If the point at 1795 Å were omitted, there would be no question of a line; as it is, we cannot rule out for certain the existence of an emission line here. We do not, however, attempt to fit a line to the three points, just note that their presence may slightly affect our accuracy in measuring the slope of the spectrum 1000–1700 Å.

No evidence is found of a spectral line at 1372 Å, suspected by K04. Although there does happen to be an upward fluctuation in the gross counts spectrum at approximately the right wavelength, it is consistent with a fluctuation in the background, and

Table 5
X-Ray Spectral Fits

Model	$N_{\rm H}$ (10^{19} cm^{-2})	kT_1 (eV)	R_1 (km)	kT_2 (eV)	R_2 (km)	Γ	A[a]	χ^2/dof
BB+PL	7	216(2)	0.073(3)	. . .	. . .	2.699(19)	1.28(3)	646/629
BB+BB	7	286(5)	0.045(5)	108(3)	0.35(4)	. . .	. . .	1084/629
BB+BB+PL	7	258(12)	0.044(7)	141(13)	0.112(15)	2.69(4)	1.05(4)	598/627
NSAgrav+PL	7	138(2)	0.294(12)	. . .	. . .	2.69(3)	1.05(3)	601/629
NSAgrav+NSAgrav+PL	7	140(20)	0.4(2)	30(11)	7(2)	1.9(6)	$0.31(2)^{+0.6}_{-0.2}$	599/627
BB+PL	13.9(13)	223(3)	0.065(2)	. . .	. . .	2.86(3)	1.46(4)	613/628
BB+BB+PL	8^{+5}_{-2}	$240^{+0.002}_{-10}$	$0.05^{+0.002}_{-0.04}$	125^{+60}_{-4}	$0.15^{+0.02}_{-0.1}$	$2.69^{+0.2}_{-0.08}$	1.1(2)	599/626
NSAgrav+PL	7(3)	140(14)	0.36(2)	. . .	. . .	2.68(5)	1.05(9)	599/628
NSAgrav+NSAgrav+PL	$2.5^{+2.5}_{-1.5}$	158(13)	0.24(5)	48(9)	2.2(8)	1.6(4)	0.23(19)	592/626

Notes. PL: power-law, BB: blackbody, NSAgrav: neutron star hydrogen atmosphere (non-magnetized). Numbers in parentheses show the 1σ confidence interval in the last digit(s). Models in the upper section have fixed column density, $N_{\rm H}$, and in the lower section it is allowed to vary. For NSAgrav, $T = T_{\rm eff}$, the model effective temperature (uncorrected for redshift) and the radius R of the effective emitting area.
[a] PL normalization A in units of 10^{-4} photon s^{-1} cm^{-2} keV^{-1} at 1 keV.

smaller in the final flux spectrum than either other fluctuations or the uncertainty expected for Poissonian statistics. As K04 claimed only a marginal detection, we assume it was due to a statistical fluctuation only.

3.2. X-Ray Band

We fitted the set of X-ray observations simultaneously using the X-ray analysis package *Sherpa*. The eight separate spectra were loaded, together with their corresponding response and background data. Each spectrum was grouped into bins with an S/N of least 8 for *XMM* and 5 for *Chandra*. All fits were performed on the whole data set simultaneously, with energy bounds 0.1–10 keV for *XMM* MOS, 0.6–10 keV for *XMM-Newton* PN, and 0.3–8 keV for *Chandra* ACIS data.

The results of fits with a variety of continuum models are shown in Table 5. Among others, we used the neutron star atmosphere model implemented in Xspec as "NSAgrav" for non-magnetized atmospheres (Zavlin et al. 1996). Keeping the mass fixed at 1.76 $M_\odot$ (Verbiest et al. 2008), and the radius at the default 10 km, we find a marginally better fit than with a single BB. The hot component best-fit normalization corresponds to a large distance ($d > 5$ kpc) if the emission were coming from the entire visible surface. Since the true distance is $d = 156$ pc, this suggests that the emission is coming from a region with effective radius less than 3% of the neutron star radius.

The upper limit established by Zavlin & Pavlov (1998) on the column density to PSR J0437−4715 is 1.2×10^{20} cm^{-2}, based on the X-ray spectrum of the nearby AGN. This would correspond to $E(B-V) \approx 0.02$ optical reddening (Predehl & Schmitt 1995; note that this relation shows considerable scatter, especially for low extinction). From fitting the softer *ROSAT*/PSPC spectra with BB, PL or neutron star atmosphere models yielded column densities in the range $(1-9) \times 10^{19}$ cm^{-2}. We performed two sets of fits, one with the fixed hydrogen column density of $N_{\rm H} = 7 \times 10^{19}$ cm^{-2} and a second set with the extinction free. We used the cross-sections of Morrison & McCammon (1983), as implemented in the model wabs. The effect of extinction for $E > 0.5$ keV is very small. The fit parameters we obtain are generally similar between the fixed and free extinction parameter. In Figure 10, we show one of our fits, with the NSAgrav+PL model and fitted extinction.

In Figure 11, we show the average fluxed spectrum (see Section 4), plotted with the best-fit BB+PL model. We can see that generally the PL component's photon index is not

only determined by the high-energy tail, but by a combination of this tail and the low-energy, extinction-affected data. Since the PL cannot rise so steeply into the EUV/FUV, we suspect that the X-ray spectrum is better modeled by multiple thermal components and a flatter PL. Furthermore, although the fit is formally acceptable, the majority of the χ^2 is contributed by the high S/N 0.5–2 keV range, leaving some structure in the residuals.

The variety of models tested in Table 5, all produce statistically acceptable fits, except BB+BB. We see thermal emission dominating the high S/N bulk of the spectrum with possibly further cool thermal temperatures at the low energies and PL at high energies. If we perform the fitting only for the higher energies, we find increasingly small (but poorly constrained) values of the photon index; e.g., for BB+PL fitted above 1 keV, $\Gamma = 2.2(3)$, and for PL only fitted to energies above 3, 4, and 5 keV, we find $\Gamma = 1.6(4)$, 2.0(6), and 1.6(9), respectively. Since the two-temperature atmosphere models also yield similar values of the photon index (Table 5), it is more likely a more realistic description of the high-energy spectrum.

3.3. Gamma Rays

We modeled the spectrum in the *Fermi* band by direct maximum-likelihood analysis of the calibrated photons falling near the position of PSR J0437−4715 on the sky.

In order to derive spectral models and fluxes for J0437, we followed the standard procedure for *Fermi* LAT data.[21] In particular, we modeled out emission from 1FGL sources (see Abdo et al. 2010) within an $r = 10°$ circle centered on J0437.

We derived the spectral fit to the J0437 spectrum in 0.1–4 GeV range[22] by maximizing the unbinned likelihood with the gtlike procedure. Standard background models were used to account for both Galactic and extragalactic diffuse emission as well as instrumental background. We have fitted both PL and cutoff PL [$E^{-\Gamma} \exp(-E/E_{\rm cut})$] models. Due to the limited statistics available in the data, the cutoff energy was not well constrained by the fitting, with a best-fit value of $E_{\rm cut}=1.3$ GeV, but with a broad acceptable range. We obtain best-fit $\Gamma = 2.6 \pm 0.2$ and $\simeq 2.2$, for the PL fit and the cutoff PL fit, respectively. The observed flux in 0.1–100 GeV is $2.7(8) \times 10^{-11}$ erg s^{-1} cm^{-2} (compared to the 1FGL value $2.4(7) \times 10^{-11}$ erg s^{-1} cm^{-2}). With

---

[21] See http://fermi.gsfc.nasa.gov/ssc/data/analysis/scitools/
[22] There are virtually no photons detected from J0437 above 4 GeV.

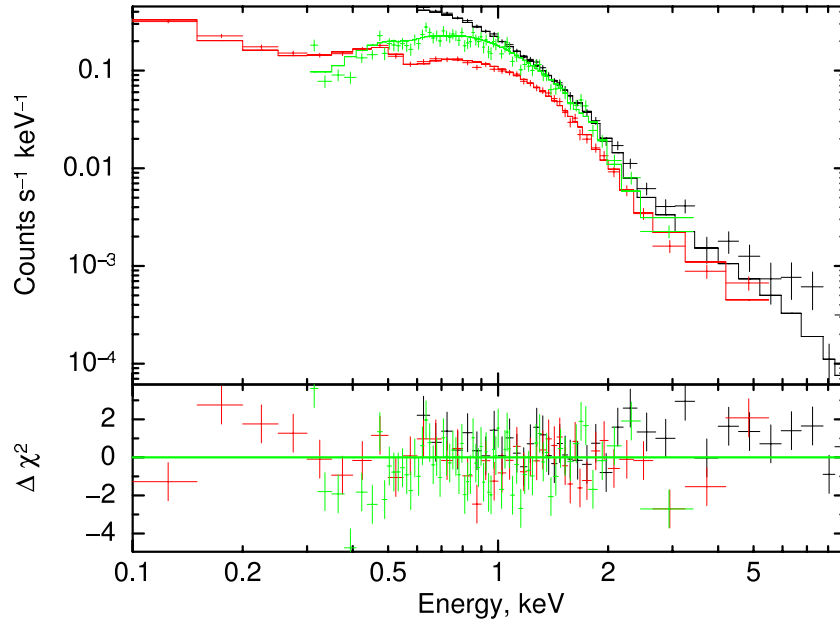**Figure 10.** Count-rate spectrum of PSR J0437−4715, with NSAgrav+PL model and $N_H = 7.4 \times 10^{19}$ cm^{-2} extinction, which had the lowest reduced chi-squared value of our fits. The black points are PN data, green is ACIS, and red is MOS1.

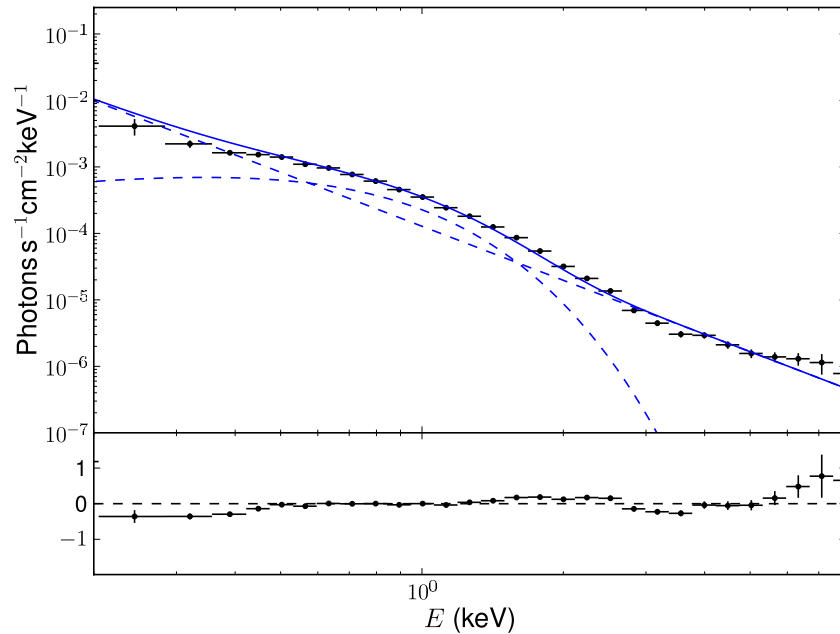(A color version of this figure is available in the online journal.)

Figure 11. X-ray BB+PL model, compared to the combined fluxed spectrum (i.e., each flux point is the weighted average of the fluxes from the three *XMM-Newton* and five *Chandra* spectra in that energy bin). The model was obtained by standard "forward fitting" of the count-rate spectra. Fractional residuals are shown in the bottom panel (i.e., (f-model)/model).

(A color version of this figure is available in the online journal.)

the statistics available it is not possible to firmly discriminate between the PL and cutoff PL models, but better S/N spectra of other MSPs suggest that cutoffs above 1 GeV are ubiquitous in MSPs (Abdo et al. 2010).

The slight difference between the fit parameters here and those listed in Abdo et al. (2010) are likely due to the larger amount of data which we analyzed.

In order to produce fluxes and uncertainties for the multi-wavelength fitting below, we spit the available energy range into five bins, and repeated the `gtlike` procedure for each bin, assuming cutoff PL.

4. MULTI-WAVELENGTH ANALYSIS

We wish to consider whether the ensemble of data across many orders of magnitude in photon energy can be fit by simple models.

We converted each spectrum into spectral energy flux, F_ν. This involves dividing the number of counts in a bin with the effective area at that particular frequency and multiplying by the bin energy. In the optical/UV regime, the effective area is simply the sensitivity function (also called zero point for photometry), but at higher energies, one normally also considers *spectral*
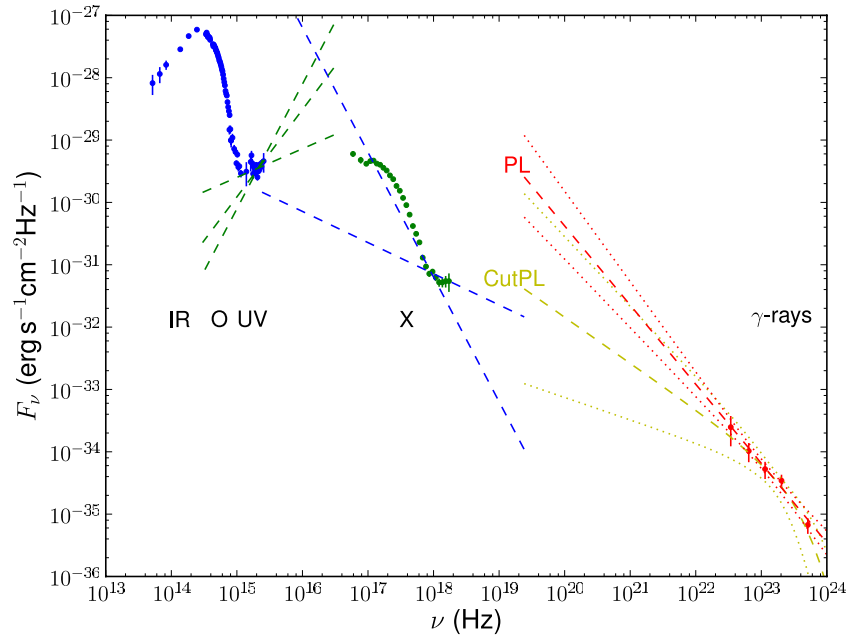
Figure 12. Multi-wavelength spectral energy distribution of PSR J0437−4715, showing the raw data (points with error bars). Overplotter are curves showing fits from the different wavebands. For the γ-ray band, we show both a cutoff PL and pure PL fits, with dashed lines for the best fits, and the 1σ confidence bounds shown with dotted lines. For the X-rays and optical–UV, we show the range of PL components from the various models, where the formal uncertainty in each PL slope is small compared to the differences between models ($\alpha = -2.5, -3.4, -4$ for the optical and $\Gamma = 1.5, 3$ for the X-ray). The thermal (pulsar and WD) components are not shown for simplicity.

(A color version of this figure is available in the online journal.)

redistribution: the number of counts in a given energy bin is determined by the incident spectral flux not only at that energy but also at other energies. Whereas in the optical this is typically only from the neighboring bins (and sets the sample spacing in spectral space), for X- and γ-rays, a photon of given energy may generate signal at a very different energy. We define the flux F in bin h as (see, e.g., Nowak 2005)

$$F_{\text{fluxed}}(h) = \frac{[C(h) - B(h)] / \Delta t}{\int R(h, E) A(E) dE}, \tag{1}$$

where $C(h)$ and $B(h)$ are the gross counts and background in bin h, $R(h, E)$ is the redistribution matrix, i.e., the normalized probability of a photon of energy E being detected in bin h, and $A(E)$ is the effective area for energy E.

In order to combine the X-ray spectra, we sample the flux from each data set in a given energy bin and take the mean weighted by the uncertainties. We note that although redistribution undoubtedly affects the appearance of narrow features, for the wide spectral range and broad bins considered here, it should make little difference.

In Figure 12, we show the multi-wavelength spectrum of PSR J0437−4715 and the fits that were made for the spectral bands separately: the IR–UV, X-rays, and γ-rays. The fits are combinations of PLs and thermal contributions, but we show only the PL components, extrapolated over many orders of magnitude, because a thermal component fitted to the X-rays, for example, does not contribute in any other spectral window. For the γ-ray fit to the *Fermi* data, there is significant uncertainty in the best-fit parameters. In order to calculate the range of spectra consistent with the models, we perform 10,000 simulations of spectra, taking parameters from Gaussian distributions with central value and spread given by the fitting; dashed lines in Figure 12 show the best-fit models, and dotted lines represent the 1σ confidence bounds. For extrapolating the X-ray and optical

spectra, the PL photon indices are very well defined for a given fit, but fits with different models give different, inconsistent values. We plot the best-fit PL components of the various models, $\Gamma = 3, 1.5$ for X-rays and $\alpha = -4, -3.4, -2.5$ for the UV. Here the value $\alpha = -4$ corresponds to a Rayleigh–Jeans law (note that $\alpha = \Gamma - 3$).

We see from Figure 12 that most of the extrapolations are not consistent between the spectral bands, with the exception of the cutoff PL in γ-rays and the flattest PL in X-rays. Note that a steep PL fit ($\Gamma = 3$) in X-rays would need to break sharply above FUV frequencies in order to connect the X-ray and FUV spectra. The PL-only fit to the *Fermi* data also appears unlikely, as it would need to turn over strongly as it approaches the X-ray band. Similarly, the PL fits to the FUV spectrum must turn over before the softest energies of the X-ray band, but this would be expected for thermal emission.

It turns out to be possible to fit simple models to the whole set of multi-wavelength spectral data. For example, in Figure 13, we have fitted a single cutoff PL across the whole range, with a number of thermal components (BBs for the UV–X-rays, and the same WD atmosphere as before in the IR/optical). Since in this case, the WD part is fixed, we only fit for frequencies $\nu > 9 \times 10^{14}$ Hz ($\lambda < 3300$ Å). The optical reddening is fixed $E(B - V) = 0.03$ and the X-ray extinction $N_{\text{H}} = 7 \times 10^{19}$ cm^{-2}. We find that the entire pulsar spectrum (excluding WD) is reasonably well fit ($\chi_\nu^2 \approx 1.2$) by a single cutoff PL and three BBs. The fit parameters are given in Table 6 (see also Figure 13). The uncertainty on the coolest temperature is small because that component contributes in both the FUV and soft X-rays, whereas in principle additional thermal components could be included in the fit; we note that the radius for this component is somewhat too small for a neutron star. With the gap in the spectrum between the FUV and soft X-rays, we are thus not able to constrain the surface temperature better than in Section 3.1.3, 1.25×10^5 K $\leqslant T \leqslant 3.5 \times 10^5$ K. Further data at the softest
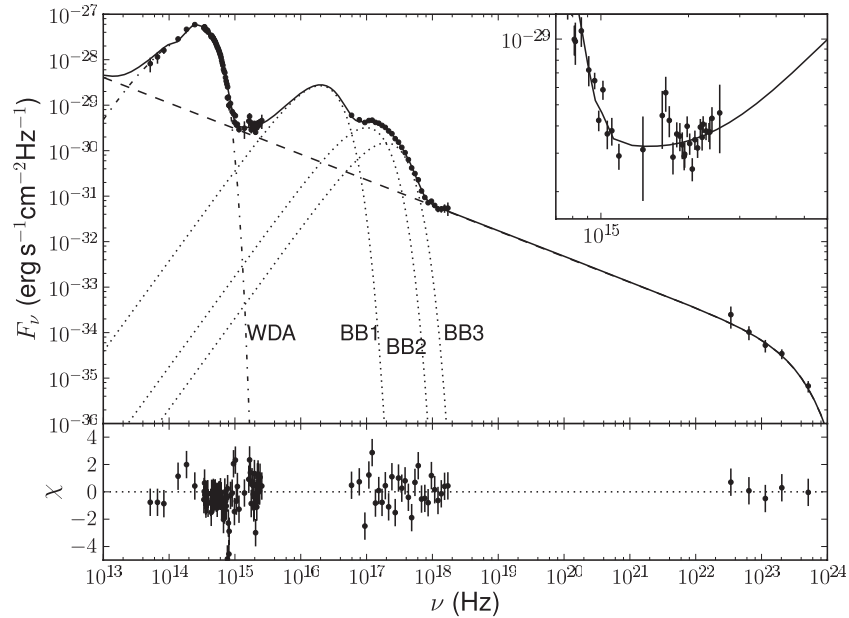
Figure 13. Multi-wavelength fit to the spectral energy distribution of PSR J0437−4715, with WD atmosphere model, blackbodies (labeled BB), and a cutoff power law ($\Gamma = 1.563(11)$, $\nu_{\rm cut} = 2.7(5) \times 10^{23}$ Hz). The inset shows a zoom of the UV part of the spectrum.

Table 6
Multi-wavelength Fits

Fit	$T_{\rm BB}$ (10^6 K)	$R_{\rm BB}$ (km)	Γ	$F_\nu (10^{23}$ Hz)	Other Parameters	χ^2/dof
CutPL+3BB	3.37(9),1.70(5),0.34(2)	0.039(4),0.160(13),5.3(8)	1.562(13)	0.99(18)	$\nu_{\rm cut} = 2.7(6) \times 10^{23}$ Hz	79/54
VarPL+3BB	3.36(7),1.66(4),0.0285(15)	0.040(5),0.168(10),76(4)	1.893(16)	3.9(6)	$b = 0.05$ (fixed)	130/55
VarPL+3BB	3.35(7),1.69(4),0.337(12)	0.039(6),0.160(11),5.2(8)	1.73(3)	3.0(4)	$b = 0.013(2)$	93/54

Notes. Blackbody and power-law fit parameters for multi-band models: CutPL (cutoff PL) and VarPL (PL with a variable index, see the text). Numbers in parentheses indicate 1σ uncertainties in the final digit(s). For the VarPL fits, $\Gamma = a + 1$.

X-ray energies (<0.2 keV) and/or an independent measurement of the X-ray extinction would be very useful. The latter could possibly be obtained from measures of photoelectric edges in high-resolution grating spectra (e.g., Durant & van Kerkwijk 2006).

We find that thermal emission from the bulk of the neutron star surface, with a temperature of 1.5×10^5 K, is supported by the data. Furthermore, we have derived a rough temperature distribution on the surface of the neutron star, largely cool, but with a much hotter polar cap (or caps). In this model, it seems plausible that the cutoff PL, which can describe the γ-ray emission adequately, is a continuation of the same PL detected in the X-rays, and which indeed also makes a contribution in the NUV range.

An alternative to the cutoff PL above could be a variable-index PL; e.g., we know from multi-wavelength observations of young pulsars that the spectrum often softens with increasing energy (Kargaltsev & Pavlov 2007), which can be modeled as

$$F_\nu = N \nu_{23}^{-a-b \log \nu_{23}}, \qquad (2)$$

where $\nu_{23} = (\nu/10^{23}$ Hz). This model has the advantage of producing a near flat F_ν in the optical regime, as is seen for non-recycled pulsars with higher $\dot{E}$ but steeper at higher energies.[23] In our case, we can either require the PL component to contribute only in γ-rays and X-rays by fixing $b = 0.05$ (Figure 14), in

which case $a = 0.89(2)$ (see Table 6). If we allow b to vary, the best-fit curvature is $b = 0.013(3)$ and the remainder of the parameters tend toward those for the cutoff PL fit. Both of the variable-index fits give statistically worse χ^2 than the cutoff PL above.

5. DISCUSSION

With the amount of multi-wavelength (MW) data gathered and analyzed, J0437 has the most comprehensive MW spectrum of an MSP to date. Also, we have measured the mid-IR–NUV spectrum of the WD companion, where, thanks to the precisely determined distance, mass, and full spectral energy distribution, the WD is one of the best-characterized WDs known.

5.1. WD Companion

The modeling in Section 3.1.2 demonstrates the high accuracy of the latest WD atmosphere models. We find that the WD has a radius $R = (1.87 \pm 0.20) \times 10^4$ km and temperature $T = 3950 \pm 150$ K and a hydrogen surface, for a WD of mass $M = 0.254\,M_\odot$. It is one of the coolest WDs observed to date (e.g., Gates et al. 2004; Hall et al. 2008; Kilic et al. 2010).

The WD radius is about 40% larger than the theoretical zero-temperature, zero-rotation radius expected for a pure-He WD (Hamada & Salpeter 1961; Driebe et al. 1998). This can be seen as a result of the non-zero-temperature hydrogen envelope and the unknown rotation rate. Very high internal magnetization ($B \sim 10^{12}$ G) of the WD (where the surface field is only a

---

[23] An exponential cutoff is still expected in the GeV range, but with the steeper model spectrum, the fit is no longer sensitive to it for our data.

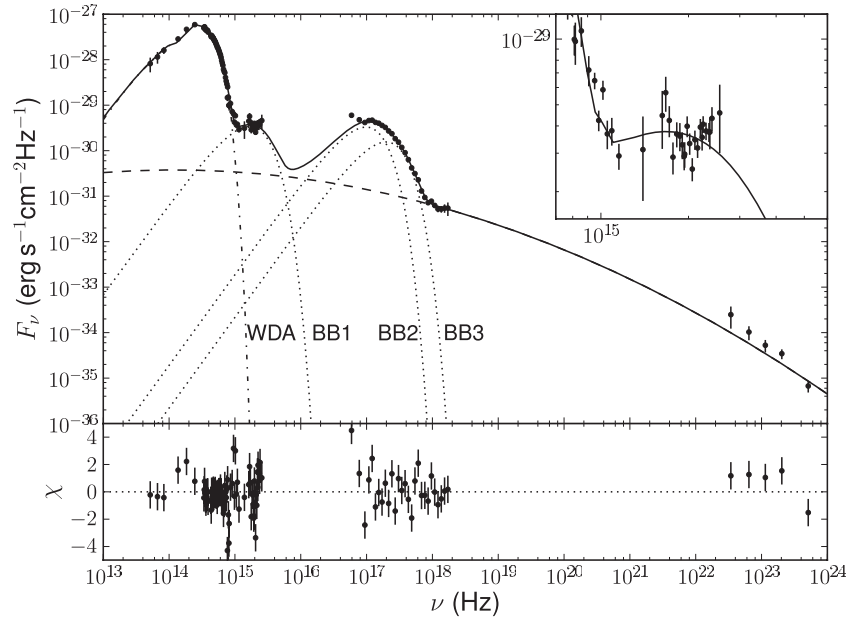**Figure 14.** Multi-wavelength fit to the spectral energy distribution of PSR J0437−4715, with WD atmosphere model, blackbodies (labeled BB), and a variable-index PL ($a = 0.89$, $b = 0.05$ in Equation (2)). The inset shows a zoom of the UV part of the spectrum.

small fraction of the interior field strength) could also result in an additional radius increase of up to 10% (Suh & Mathews 2000).

Hansen & Phinney (1998) considered the PSR J0437−4715 system in detail, in order to derive limits on the age and initial pulsar spin period (since the cessation of accretion). The temperature, surface composition, and mass of the WD companion to PSR J0437−4715 can be used to derive an estimate on its age. Using Figure 2 of Hansen & Phinney (1998), we estimate $\tau_{WD} = 6.0 \pm 0.5$ Gyr. For a 0.242 $M_\odot$ mass WD, Serenelli et al. (2001) also predicted a surface temperature and colors consistent with our findings after 6 Gyr.

It is interesting to compare the inferred WD age with the pulsar age. A correction must be applied to the apparent characteristic age of the pulsar, caused by the transverse Doppler effect due to the pulsar's transverse velocity (i.e., proper motion; Shklovskii 1970). For the particular case of PSR J0437−4715, being close to us and having a large proper motion, this correction is significant. Specifically, the Shklovskii correction to the characteristic rate for proper motion, μ, and distance, D, is given by $(\dot{P}/P)_i = (\dot{P}/P) - \mu^2 D/c$, where the subscript i denotes the intrinsic value. Using the precise VLBI measurements of μ and D by Deller et al. (2008), we find the corrected spin-down characteristic age is $\tau_{PSR} = P/\dot{P}_i(n-1)[1 - (P_0/P)^{n-1}] = 6.7 \pm 0.2$ Gyr, assuming breaking index $n = 3$ and spin period $P_0 \ll P = 5.8$ ms.

The derived ages are rather similar with one another, surprising given the number of assumptions involved. This implies P_0 must be substantially faster (at least a factor of 1.4 for $n = 3$) than the current period of 5.8 ms (cf. 1.4 ms for the fastest known pulsar; Hessels et al. 2006).

5.2. Pulsar Thermal Emission

We have constrained the temperature of the bulk of the pulsar surface to 1.25×10^5 K $\leqslant T \leqslant 3.5 \times 10^5$ K for reasonable radii, or 1.5×10^5 K for the preferred radius of 13 km, with about a 15% uncertainty dominated by the uncertainty in the extinction.

The range of allowed temperatures could be further constrained if data in the gap between FUV and X-rays becomes available.

It is obvious from our MW fits that the thermal component cannot be described well by a single BB or NS atmosphere model, supporting the conclusions of Zavlin & Pavlov (1998) and Zavlin et al. (2002). The large width of the thermal peak argues strongly in a favor of multi-temperature thermal spectrum, which would be the natural consequence of a non-uniformly heated NS surface. If modeled as a sum of BBs, the observed spectrum requires a high-temperature ($\simeq 4$ MK) component that appears to be emitted from a relatively small area and it also requires a cooler component that must be radiated from most of the NS surface. Hence, one could suggest that the hot component comes from heated polar caps (see K04 and references therein) while the cool component is due to the residual heat stored in the NS interior. However, the temperature of this cooler component, $\simeq 0.15$ MK, is surprisingly large for a passively cooling NS. This means that either a heating mechanism operates in the NS interior or the heat deposited at the polar caps is efficiently conducted to the rest of the NS surface. In modeling the phase-resolved spectrum, Bogdanov et al. (2007) suggest some axial asymmetry for the hotter components explained by an offset dipole magnetic field.

5.2.1. Heating Mechanisms

After an initial neutrino-dominated cooling epoch, passive photon-dominated cooling from the NS surface is expected to rapidly reduce the surface temperature to below 10^5 K by 1 Myr, and 10^3 K by 1 Gyr (see the review by Yakovlev & Pethick 2004 and Page et al. 2006). The surface temperature we find is well above this. There may be a number of possible mechanisms for internal re-heating of the NS which can result in higher surface temperatures of very old pulsars. Such mechanisms are discussed in Page et al. (2006), but we briefly summarize several of the relevant possibilities here.

1. The interior of the NS is thought to contain superfluid, so, as the crust spins down, differential rotation will be created between the layers, and this can release energy by

16

the friction between the "creeping" superfluid vortex lines and the non-superfluid crust to which it is pinned (Larson & Link [1999]). Similar processes are thought to be responsible for the well-known glitching behavior of younger pulsars. In late times ($\tau \gg 10^6$ yr), the photon cooling from the NS surface balances the frictional heating, and the thermal luminosity, independent of the previous NS thermal history, is equal to the spin-down rate multiplied by the excess angular momentum in the core with respect to the crust, $L = J|\dot{\Omega}|$. Larson & Link ([1999]) used this to explain the temperatures of three moderately old ($\tau \sim 10^7$ yr) pulsars.

2. Ohmic heating due to currents induced by the NS magnetic field (Aguilera et al. [2008]). This effect is only relevant for high-B NSs. Although the initial field may have been much higher than it is today, all MSPs have weak surface magnetic field, presumably due to processes in the accretion phase. Stronger fields may, in principle, be buried in the NS interior, so we cannot completely exclude ohmic heating.

3. The centrifugal force of rapid rotation affects the chemical balance in the NS interior. As the NS spins down, the force decreases, and the particle populations are forced into non-equilibrium. Chemical reactions restoring this equilibrium will release heat, a process known as rotochemical heating (Reisenegger [1995]). For the surface temperature for J0437 reported by K04, Petrovich & Reisenegger ([2010], [2011]) developed a specific model for heating in this case and concluded that rotochemical heating was the preferred heating mechanism. Our surface temperature range is slightly higher than that given by K04 moving J0437 slightly further from the rotochemical model cooling curve, but not significantly enough to alter Petrovich & Reisenegger's ([2010]) conclusions.

4. With the high mass and density of an NS, it is possible that dark matter particles could be trapped there and either decay or annihilate, releasing energy (Kouvaris [2008]; Bertone & Fairbairn [2008]). The nature of dark matter particles is currently unknown, so the quantitative predictions of such a mechanism remain rather uncertain. Dark matter, even if it liberates both gravitational and rest-mass energy, probably has far too low a density in the solar neighborhood to contribute significantly to PSR J0437's 10^5 K surface emission (Kouvaris & Tinyakov [2010]).

Both vortex creep and rotochemical heating mechanisms depend on rotational kinetic energy. According to Gonzalez & Reisenegger ([2010]), only these two mechanisms will be important at timescales comparable to PSR J0437's age. Our measurement of the bulk surface temperature, 1.25×10^5K $\leqslant T \leqslant 3.55 \times 10^5$ K, is more precise and slightly higher than the temperature found by K04. Although the allowed range of surface T is in agreement with the more uncertain K04 measurement, we stress that the important result of our analysis is a much increased confidence in the thermal interpretation of the pulsar FUV spectrum (K04 allowed for a non-thermal interpretation as well).

The relationship between the NS mass, radius, and temperature structure (or, equivalently, density, pressure, and temperature) is generally termed the equation of state (EoS). We have constrained the (bulk) surface temperature and the function of radius versus surface temperature. However, in order to make a statement about the EoS, assumptions must be made about the internal temperature profile. Such a profile depends upon the internal heating model, and thus constraints on the EoS are model-dependent. For example, Petrovich & Reisenegger ([2010]) show

that, in the rotochemical heating scenario, any temperature of order 10^5 K requires superfluidity, and our measurement constrains their superfluidity parameter 0.1 MeV $< \Delta_{th} < 0.2$ MeV for the A18 + δv + UIX*, one EoS considered.

5.2.2. Polar Cap Heating

As well as residual heat in the interior and any heating mechanism discussed above, the surface temperature profile of the pulsar will be affected by the energetics of spin-down induced magnetospheric activity. A large amount of energy is available from the loss of rotational kinetic energy, $\dot{E}_i = 2.8 \times 10^{33}$ erg s^{-1}, but the majority of this will be released as a relativistic wind. Some fraction of this power is, however, released as magnetospheric photon emission (which accompany the particle cascades). High-energy magnetospheric particles are responsible for the non-thermal emission from the pulsar, but it is generally believed that some fraction of the particle flux returns to the NS surface along the field lines, heating the polar caps. Indeed, this is believed to be the cause of soft X-ray thermal emission with $T \gtrsim 10^6$ K and projected areas much smaller than the size of an NS (Harding [2007]). In the case of J0437, it is reasonable to assume that the hotter BB components fitted above, with a combined luminosity of $L_{hot} \sim 10^{30}$ erg s^{-1}, are also polar caps heated in a similar way to other pulsars. The thermal X-ray efficiency of the order $\eta \approx 3 \times 10^{-4}$ is within the expected range (Gil et al. [2007]; Kargaltsev & Pavlov [2008]).

Harding ([2007]) reviews the production of particles and radiation in the vicinity of pulsars, and polar cap heating from different polar cap emission models. Their models for MSPs predict a luminosity similar to that which we find for the "hot" luminosity, L_{hot}. Given that these particles will not penetrate beneath the atomic layers (Datta et al. [1995]), we expect the downward particle flux to have a negligible effect on the temperature observed for the bulk of the NS surface. Heat may, however, propagate along the surface if the conductivity is high enough, and this is suggested by the broadness of the thermal spectral peak. According to the fits in Table 6, however, the hot polar cap is small, and the temperatures intermediate between the hottest areas and the bulk of the neutron star surface are emitted from an area still small compared to the total. We therefore infer that the conduction along the surface is probably small.

In short, the surface temperature 1.25×10^5 K $\leqslant T \leqslant 3.5 \times 10^5$ K is unlikely to be affected by magnetospheric processes, and therefore reflects the internal thermal evolution of the pulsar. Furthermore, the spectrally broad thermal emission can be resolved into a function of temperature versus emitting area (see Figure [13]), which can then be used to constrain the heat conduction in the surface layers, once such models become available.

5.3. Magnetospheric Emission

The multi-wavelength data suggest that a single non-thermal component may be responsible for emission from the UV to GeV energies. Whether this is indeed a single PL, with a high-energy cutoff, or a variable exponent would best be determined by filling in the spectral window between 10 keV and 0.1 GeV, which may become feasible with upcoming facilities such as *NuStar*. The possible rising PL tail at low energies in Figure [13] raises the intriguing possibility of observing the source with ALMA. Unfortunately, MIPS on board *Spitzer* is no longer operational, and the data presented here offer no constraint on the PL in the mid-IR.

The GeV luminosity observed is 8×10^{31} erg s^{-1} (100 MeV–100 GeV, which contains most of the non-thermal luminosity

as estimated from Figure 13). This gives a magnetospheric radiation efficiency $\eta = L_\gamma/\dot{E} \approx 0.03$. This is within the typical range for *Fermi*-detected pulsars (Abdo et al. 2009).

The non-thermal emission in GeV appears to be 100% pulsed (Abdo et al. 2010). In the X-ray range, the pulsed fraction increases with energy from 30% at 0.3 keV to over 50% for 2–6 keV (Zavlin 2006; Bogdanov et al. 2007). This can be explained by a combination of weakly pulsed thermal component with a smooth pulse profile, and a highly pulsed magnetospheric component with a sharper pulse profile. In detailed modeling of the energy-dependent light curve of J0437, Bogdanov et al. (2007) do not explicitly consider the role of the PL component. They do remark, however, that the pulse profile for the PL alone must not be too sharp, otherwise its effect would also be seen in the light curves at lower energies, where thermal emission dominates. If the PL photon index were sufficiently flat ($\Gamma < 2$), then the latter restriction could be lifted.

Under the assumption that the non-thermal emission is indeed a single PL component, how plausible is such a broadband PL? Assuming that we are seeing synchrotron emission from FUV to ~ 1 GeV, a broad range of particle energies and/or magnetic field strengths must be present. There are two boundary energies: the energy of PL break (~ 1 GeV) and the lowest energy observed (~ 1 eV). With primary particles capable of radiating at up to 1 GeV energies, a population of lower-energy secondary particles will be created, which can emit synchrotron radiation. The photon energy emitted at the light-cylinder magnetic field (where the dipolar field is the weakest), $B_{LC} = 3 \times 10^4$ G, is approximately $E_{syn} \sim 10^{-4} \gamma^2$ eV (where γ is the Lorentz factor). Thus a lepton population near the light cylinder with Lorentz factors in the range of about 100 to a few times 10^6 could account for PL emission from optical to GeV, with the slope of the electron energy spectrum, $p = 2\Gamma - 1 \approx 2.1$. The value of the high-energy cutoff is typical for the pulsars detected by *Fermi*, either classical or MSPs (e.g., Baring 2010), presumably because the B_{LC} is similar for both populations. As a more conventional interpretation, the γ-ray emission could be produced by the curvature radiation or primary electrons (Muslimov & Harding 2004; Harding et al. 2008), with the energy of the emitted radiation dependent on the altitude of the emitting particles. However, it has been recently pointed out by Baring (2010) that under certain conditions, the synchrotron radiation is expected to dominate.

If the NUV emission is indeed (at least partly) magnetospheric in origin, then one would expect it to be highly pulsed, in contrast to the NS and WD thermal emission in the optical and FUV. Detection of pulsations would confirm the presence of the non-thermal component over many orders of magnitude in energy. Only the STIS aboard *HST* has both the required sensitivity and time resolution for such an observation. Detection of pulsation from the ground (in the u' band) is possible, in principle, but very sensitive instrumentation would be required to disentangle the magnetospheric and thermal (both WD and pulsar) emission components. Likewise, in the (long-wavelength end of) FUV, there is no current instrument but STIS capable of time resolution high enough to measure pulsation.

Whereas non-thermal emission has been observed in the optical/NUV spectra of young pulsars such as Vela, it has not yet been found in the UV for any other old ($\tau > 1$ Gyr) pulsar. The late-age reappearance of a magnetospheric component in the optical may in principle result from two factors: the lower surface heating rate from the downward flux of magnetospheric particles and that the heating of the surface from stored internal

heat is expected to continue in young neutron stars only to ages of ~ 1 Myr. The hot thermal component is therefore much weaker in older pulsars, enabling the possible detection, as here, of both the cool thermal component from the bulk of the surface and NUV non-thermal emission.

Variable-index PLs have been used before to describe broad-band non-thermal emission in pulsars (Cusumano 2004). Young pulsars, such as the Crab and Vela, are known to emit non-thermal emission in a very broad band. For middle-aged pulsars, extrapolation of the X-ray PL components to lower frequencies commonly overpredicts the optical (Kargaltsev & Pavlov 2007). One might speculate that for those young energetic pulsars where B_{LC} is higher, the low-energy downturn of the PL falls between the optical and X-rays ($E_{low} \propto B_{LC}$), causing a break in the spectrum. On the other hand, poor modeling of the X-ray spectrum (where detailed atmospheric models may be more appropriate than simple BB models) may bias the non-thermal PL slopes measured.

When the spectral fluxes of the gamma, X-ray, and IR–UV data of several pulsars are plotted side by side, connecting the non-thermal emission with a single PL in each case does seem plausible (see Durant et al. 2011). That does not necessarily imply that a single component is responsible for 100% of the non-thermal emission, but possibly for a large fraction of it. The prospect of detecting more pulsars in the optical and improved coverage at hard X-ray energies will certainly clarify this picture in the near future.

6. SUMMARY AND OUTLOOK

We have obtained broadband spectral coverage of the binary system containing the old MSP J0437−4715. In particular, high-quality optical, UV, and X-ray spectra, supplemented with broadband coverage in the IR and GeV γ-rays, have enabled us to construct the most complete spectral energy distribution for an MSP to date, as well as accurately model the atmosphere of one of the best-observed cool WDs. The data enable us to constrain the NS surface temperature and hint at a broad magnetospheric component stretching from the NUV to GeV γ-rays.

Although PSR J0437−4715 gives an interesting data point in the $T(\tau)$ dependence, the thermal history of pulsars and the dependence of evolution on the mass and other parameters can only be found by measuring the surface temperatures of other pulsars through UV observations. A successful model for pulsar thermal evolution would constrain the EoS of the neutron star interior. Similarly, an increasing sample of detailed observations of WDs with well-determined characteristics (e.g., Parsons et al. 2011) will invariably lead to better evolutionary models.

If the extremely broad non-thermal spectral component is real, it ought to be seen by *nuSTAR* in the 10–50 keV range. Similarly, ALMA may detect the component at lowest energies, if there is no low-energy cutoff. It will be interesting to see whether similar components reveal themselves in the spectra of other millisecond and ordinary pulsars when the full multi-wavelength spectrum is analyzed. As more *Fermi* LAT data accumulate, more pulsars will be available for multi-wavelength follow-up. Multi-wavelength studies appear to be the most promising exploration tool in the coming next decade.

REFERENCES

Abdo, A. A., Ackermann, M., Ajello, M., et al. 2009, ApJ, 706, L56
Abdo, A. A., Ackermann, M., Ajello, M., et al. 2010, ApJS, 187, 460
Aguilera, D. N., Pons, J. A., & Miralles, J. A. 2008, A&A, 486, 255
Althaus, L. G., Panei, J. A., Romero, A. D., et al. 2009, A&A, 502, 207
Bailyn, C. D. 1993, ApJ, 411, L83
Baring, M. G. 2010, in AIP Conf. Proc. 1379, Astronomy of Neutron Stars 2010, ed. E. Göğüş, T. Belloni, & Ü. Ertan (Melville, NY: AIP), 74
Bassa, C. G., van Kerkwijk, M. H., & Kulkarni, S. R. 2006, A&A, 450, 295
Bell, J. F., Bailes, M., & Bessell, M. S. 1993, Nature, 364, 603
Bell, J. F., Bailes, M., Manchester, R. N., Weisberg, J. M., & Lyne, A. G. 1995, ApJ, 440, L81
Bergeron, P., Saumon, D., & Wesemael, F. 1995, ApJ, 443, 764
Bertone, G., & Fairbairn, M. 2008, Phys. Rev. D, 77, 043515
Bogdanov, S., Rybicki, G. B., & Grindlay, J. E. 2007, ApJ, 670, 668
Cardelli, J. A., Clayton, G. C., & Mathis, J. S. 1989, ApJ, 345, 245
Cusumano, G. 2004, Adv. Space Res., 33, 495
Danziger, I. J., Baade, D., & della Valle, M. 1993, A&A, 276, 382
Datta, B., Thampan, A. V., & Bhattacharya, D. 1995, JA&A, 16, 375
Deller, A. T., Verbiest, J. P. W., Tingay, S. J., & Bailes, M. 2008, ApJ, 685, L67
Dolphin, A. E. 2000, PASP, 112, 1383
Driebe, T., Schoenberner, D., Bloecker, T., & Herwig, F. 1998, A&A, 339, 123
Durant, M., Kargaltsev, O., & Pavlov, G. G. 2011, ApJ, 743, 38
Durant, M., & van Kerkwijk, M. H. 2006, ApJ, 650, 1082
Fazio, G. G., Hora, J. L., Allen, L. E., et al. 2004, ApJS, 154, 10
Gates, E., Gyuk, G., Harris, H. C., et al. 2004, ApJ, 612, L129
Gil, J., Melikidze, G., & Zhang, B. 2007, MNRAS, 376, L67
Gonzalez, D., & Reisenegger, A. 2010, A&A, 522, A16
Hall, P. B., Kowalski, P. M., Harris, H. C., et al. 2008, AJ, 136, 76

Hamada, T., & Salpeter, E. E. 1961, ApJ, 134, 683
Hansen, B. M. S., & Phinney, E. S. 1998, MNRAS, 294, 569
Harding, A. K. 2007, arXiv:0710.3517
Harding, A. K., Stern, J. V., Dyks, J., & Frackowiak, M. 2008, ApJ, 680, 1378
Hessels, J. W. T., Ransom, S. M., Stairs, I. H., et al. 2006, Science, 311, 1901
Horne, K. 1986, PASP, 98, 609
Kargaltsev, O., & Pavlov, G. 2007, Ap&SS, 308, 287
Kargaltsev, O., & Pavlov, G. G. 2008, in AIP Conf. Proc. 983, 40 Years of Pulsars: Millisecond Pulsars, Magnetars and More, ed. C. Bassa, Z. Wang, A. Cumming, & V. M. Kaspi (Melville, NY: AIP), 171
Kargaltsev, O., Pavlov, G. G., & Romani, R. W. 2004, ApJ, 602, 327
Kilic, M., Munn, J. A., Williams, K. A., et al. 2010, ApJ, 715, L21
Kouvaris, C. 2008, Phys. Rev. D, 77, 023006
Kouvaris, C., & Tinyakov, P. 2010, Phys. Rev. D, 82, 063531
Kowalski, P. M. 2006, ApJ, 641, 488
Kowalski, P. M., Mazevet, S., Saumon, D., & Challacombe, M. 2007, Phys. Rev. B, 76, 075112
Kowalski, P. M., & Saumon, D. 2004, ApJ, 607, 970
Kowalski, P. M., & Saumon, D. 2006, ApJ, 651, L137
Kümmel, M., Walsh, J. R., Pirzkal, N., Kuntschner, H., & Pasquali, A. 2009, PASP, 121, 59
Larson, M. B., & Link, B. 1999, ApJ, 521, 271
Lattimer, J. M. 2010, New Astron. Rev., 54, 101
Martini, P., Persson, S. E., Murphy, D. C., et al. 2004, Proc. SPIE, 5492, 1653
Morrison, R., & McCammon, D. 1983, ApJ, 270, 119
Muslimov, A. G., & Harding, A. K. 2004, ApJ, 617, 471
Nowak, M. 2005, Ap&SS, 300, 159
Page, D., Geppert, U., & Weber, F. 2006, Nucl. Phys. A, 777, 497
Parsons, S. G., Marsh, T. R., Gänsicke, B. T., Drake, A. J., & Koester, D. 2011, ApJ, 735, L30
Petrovich, C., & Reisenegger, A. 2010, A&A, 521, 77
Petrovich, C., & Reisenegger, A. 2011, A&A, 528, A66
Predehl, P., & Schmitt, J. H. M. M. 1995, A&A, 293, 889
Reach, W. T., Megeath, S. T., Cohen, M., et al. 2005, PASP, 117, 978
Reisenegger, A. 1995, ApJ, 442, 749
Rieke, G. H., Young, E. T., Engelbracht, C. W., et al. 2004, ApJS, 154, 25
Sarna, M. J., Ergma, E., & Gerskevits, J. 2001, Astron. Nachr., 322, 405
Saumon, D., & Jacobson, S. B. 1999, ApJ, 511, L107
Seaton, M. J. 1979, MNRAS, 187, 785
Serenelli, A. M., Althaus, L. G., Rohrmann, R. D., & Benvenuto, O. G. 2001, MNRAS, 325, 607
Shklovskii, I. S. 1970, SvA, 13, 562
Sirianni, M., Jee, M. J., Benítez, N., et al. 2005, PASP, 117, 1049
Suh, I., & Mathews, G. J. 2000, ApJ, 530, 949
Trilling, D. E., Mueller, M., Hora, J. L., et al. 2008, ApJ, 683, L199
van Kerkwijk, M. H., & Kulkarni, S. R. 2001, A&A, 378, 986
Verbiest, J. P. W., Bailes, M., van Straten, W., et al. 2008, ApJ, 679, 675
Walkowicz, L. M., Johns-Krull, C. M., & Hawley, S. L. 2008, ApJ, 677, 593
Yakovlev, D. G., & Pethick, C. J. 2004, ARA&A, 42, 169
Zavlin, V. E. 2006, ApJ, 638, 951
Zavlin, V. E., & Pavlov, G. G. 1998, A&A, 329, 583
Zavlin, V. E., Pavlov, G. G., Sanwal, D., et al. 2002, ApJ, 569, 894
Zavlin, V. E., Pavlov, G. G., & Shibanov, Y. A. 1996, A&A, 315, 141